Triplet Down Conversion using Optical Phase Space Methods

Author
Mathew Denys

Supervisor
Dr. Ashton Bradley

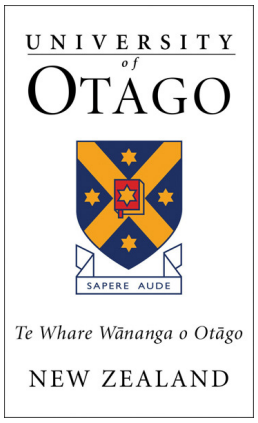

September 2018

Abstract

Triplet down conversion is a non-linear optical process which was first achieved experimentally in 2010. The highly non-linear interaction poses challenges for a theoretical treatment of the process. In this dissertation, the positive-P representation of optical phase space is used to examine the time evolution of a system undergoing triplet down conversion, with a focus on the degenerate case. We examine the behaviour of the resulting steady states as a function of the pumping that drives the interaction, and use these to identify regimes of entanglement and squeezing that should provide a guide for future experimental efforts. A comparison of the positive-P method to a simulation in a number state basis is performed in order to examine the validity of the positive-P methods implemented. Non-degenerate triplet down conversion is also considered as a more general case.

Student Contribution

The work presented in this dissertation is primarily my own, but has been assisted by various sources. Here I briefly distinguish between what I have contributed, and where I have received help or followed other work closely.

The backbone of my work involved solving the system of stochastic differential equations (1.59), and later (4.2). The code used to solve these equations was provided by Ashton Bradley, and significantly modified by myself as required. All other code was written solely by myself, although it should be noted that the code used for the Monte Carlo wave function simulations in Chapter 5 was heavily influenced by example code in the `QuantumOptics.jl` documentation[1].

There are some important results throughout this dissertation which replicate the results of other work. In Chapter 2, the time evolution presented in Figure 2.1 is an independent replication and validation of the work of *Olsen* [1]. The same applies to the removal of pumping (Figure 2.3), but I include an additional original result here where I began the system away from the vacuum. The analytic derivation presented in Section 2.3.1 reproduce the results from the work of *Bajer* [2] using a different formalism. The corresponding numerical work in Section 2.3.1 is entirely original. The results of Sections 3.1 and 3.2, and Chapter 4 also independently replicate *Olsen's* work.

The core results of this dissertation are presented in Sections 2.3.2 and 3.3, and are entirely my own. All the work in Chapter 5 is original, as is the discussion of numerics in Appendix B.

[1] See https://qojulia.org/documentation/examples/jaynes-cummings.html#Jaynes-Cummings-model-1.

Acknowledgements

First and foremost I would like to thank Dr. Ashton Bradley for his expertise and guidance throughout this year. Not only have you managed to pass on a lot of knowledge to me, but also enthusiasm and excitement for what I was doing. My appreciation also to all academic and support staff members of the Physics department who I have interacted with this year, including my examiners who have provided me with important feedback.

Thanks also go of course to my family. To my Dad for managing not only to read through my progress report and dissertation, but to also provide valuable feedback - I hope you got something out of them, and to my Mum for being someone I could talk things through with when they were a bit rough.

A big thank you to all my friends, both those in the department and those from other areas of my life. It's hard to quantify the effect that having people to relax with over lunch or in the evenings and weekends can have on my enjoyment and productivity. Particular thanks go to Josephine for being so incredibly supportive, and to George for not dying a few weeks before hand in despite trying his best - the lack of emotional trauma probably helped me reach a finished product.

Contents

Chapter 1

Introduction

Triplet down conversion is the non-linear optical process of "splitting" one photon into three. In order to obtain a strong interaction, experimental realisation of the process usually takes place within an optical cavity - such as a whispering gallery mode resonator - that contains a $\chi^{(3)}$ crystal as a non-linearity. High energy photons are supplied to the resonator, and the existence of the non-linearity allows them to be down converted to lower energy photons. Triplet down conversion was first observed experimentally as early as 2010 [3], and has interest due to its possible generation of squeezed light, and more recently for its applications to quantum information [4, 5]. To date there has been no experimentally measurable quantum entanglement as a result of triplet down conversion. Theoretical analyses typically implement optical phase space methods to describe the process, which unfortunately introduce errors. Comparisons of various phase space techniques can be found in the literature [6], but no comparisons have been made to more exact approaches.

I have investigated triplet down conversion using the positive-P representation of optical phase space. The work presented here primarily focuses on degenerate down conversion, in which the down converted photons are indistinguishable. This means that there are only two fields of interest - a high energy, "pumped", mode and a low energy, "down-converted", mode. The time evolution of the fields is modelled by a set of coupled stochastic differential equations which will be derived in Section 1.5, along with a more in depth discussion of the process of triplet down conversion. First however, this dissertation begins with an overview of some core ideas pertaining to the representation of systems in optical phase space, and the modelling of stochastic processes. The presentation of my results begins in Chapter 2, where I investigate the time evolution of the mode populations and the steady states that they are found to reach. A focus is placed on a systematic investigation of the role that pumping plays in the interaction, with has been partially examined in [2], but without the full inclusion of quantum noise. Chapter 3 examines the fluctuation spectra of the steady state, focussing on the squeezing and entanglement of the output fields. In Chapter 4 we consider the more general case of non-degenerate down conversion, in which the down converted photons are distinguishable. This results in four distinct modes - one pumped, and three down converted, that can in general be in a quantum entangled state. Finally, Chapter 5 compares the phase space results to simulations using a Monte Carlo wave function approach. This has not been done before, and provides an important test of the validity of the positive-P method for this system. A list of notation used throughout this work can be referenced in Appendix A.

1.1 Review of Quantum Mechanics

States: In quantum mechanics, the possible states of a system are described by kets, which belong to a Hilbert space. For example, $|\psi\rangle$ denotes the state identified by the label ψ. The associated Dual vector, $\langle\psi|$, is called a bra. The inner product between a bra and a ket, $\langle\phi|\psi\rangle$, is a c-number[1] with the following properties:

$$\langle\phi|\psi\rangle = \langle\psi|\phi\rangle^*, \qquad 1 \geq \langle\psi|\phi\rangle \geq 0, \qquad \langle\psi|\psi\rangle = 1. \tag{1.1}$$

It represents the projection of $|\psi\rangle$ onto the state $|\phi\rangle$, and is physically interpreted as the probability amplitude of a system in the state $|\psi\rangle$ being measured to be in the state $|\phi\rangle$. The actual probability of measuring the system in $|\phi\rangle$ is given by $|\langle\phi|\psi\rangle|^2$.

Operators: An operator, $\hat{A}$, acts on kets by mapping them to different kets in the same Hilbert space. All operators have an "adjoint", their conjugate transpose, which satisfies

$$\hat{A}\,|\psi\rangle = |\phi\rangle \iff \langle\psi|\hat{A}^\dagger = \langle\phi|\,. \tag{1.2}$$

In certain cases $\hat{A}$ will be its own conjugate transpose, i.e. $\hat{A}^\dagger = \hat{A}$, in which case it is said to be self-adjoint, or *Hermitian*. All observables (anything that can be measured) are represented by Hermitian operators, and all possible outcomes of a measurement of an observable are given by the eigenvalues of the corresponding operator. Non-Hermitian operators also exist in quantum mechanics, and will be used in this work, but do not represent observables. The expectation value of a measurement of the operator $\hat{A}$ on the state $|\psi\rangle$ is denoted by $\langle\hat{A}\rangle$, which is shorthand for the full expression

$$\langle\hat{A}\rangle_\psi = \langle\psi|\hat{A}|\psi\rangle\,. \tag{1.3}$$

Bases: A ket can be written as a linear combination of basis states, which can be discrete of continuous. In a discrete basis we can think of kets and bras as column and row vectors respectively, and operators as matrices. A basis is said to be *orthonormal* if its basis kets satisfy

$$\langle i|j\rangle = \delta_{ij}, \tag{1.4}$$

and *complete* if the basis kets span the entire Hilbert space, which is to say

$$|\psi\rangle = \sum_i |i\rangle\langle i|\psi\rangle \equiv \sum_i c_i\,|i\rangle\,, \tag{1.5}$$

for any ket $|\psi\rangle$ in the Hilbert space. If a basis is complete *and* orthonormal we have $\sum_i |c_i|^2 = 1$, and the identity operator is given by

$$\mathbb{1} = \sum_i |i\rangle\langle i|\,. \tag{1.6}$$

[1] A c-number is simply a complex number. The explicit naming is in order to differentiate them from operators.

For a continuous basis, $|\langle\phi|\psi\rangle|^2$ is a probability density rather than a true probability, and (1.4) - (1.6) are respectively given by

$$\langle x|x'\rangle = \delta(x-x'), \qquad |\psi\rangle = \int dx\, |x\rangle\langle x|\psi\rangle \equiv \int dx\, \psi(x)\, |x\rangle\,, \qquad \mathbb{1} = \int dx\, |x\rangle\langle x|\,. \tag{1.7}$$

Later in this work we deal with bases that are not orthonormal, in which case the identity takes a different form.

Time Evolution: Finally, the time evolution of a ket is governed by the Schrödinger equation,

$$i\hbar\frac{\partial}{\partial t}\,|\psi(t)\rangle = \hat{H}\,|\psi(t)\rangle\,, \tag{1.8}$$

where $\hat{H}$ is the Hamiltonian operator. As we see below, there are alternative ways to consider the time evolution of a quantum system.

1.2 The Density Matrix

The density matrix, ρ, is often used to describe the statistical state of a quantum system, especially when we do not know the exact quantum state of the system, such as when we are dealing with mixed states. It is defined in terms of a discrete basis as

$$\rho = \sum_n P_n\, |\psi_n\rangle\langle\psi_n|\,, \tag{1.9}$$

where P_n is the probability that the system is in the pure state $|\psi_n\rangle$. The density matrix provides a representation of the uncertainty in a system: the outer products account for the inherent quantum mechanical uncertainty of the quantum state $|\psi_n\rangle$, while the P_n accounts for any uncertainty as to which quantum state the system is in. Some useful properties are:

1. The expectation value of an operator acting on the system is

$$\langle\hat{A}\rangle = \mathrm{Tr}[\hat{A}\rho], \tag{1.10}$$

   where $\mathrm{Tr}[\,\cdot\,]$ denotes the trace operation, defined as $\mathrm{Tr}[\hat{A}] = \sum_j \langle j|\,\hat{A}\,|j\rangle$. It is this property that gives the density matrix its name, as a (conditional) probability density plays the analogous role in classical systems.

2. The trace of the density matrix is unity,

$$\mathrm{Tr}[\rho] = 1. \tag{1.11}$$

3. The density matrix is Hermitian,

$$\rho^\dagger = \rho. \tag{1.12}$$

1.2.1 Closed and Open Systems

Before discussing the time evolution of the density matrix, we make a brief aside. A closed system is one which is completely isolated from everything else, while an open system is one which is in "contact" with some other system. In the case that the other system is much larger than the system of interest, we generally call it a *reservoir* or *the environment*. The distinction between a closed and open system is important, because some formalisms only apply to closed systems. In the context of triplet down conversion, the system of interest is an optical resonator, which is an open system as it can exchange photons with the environment. The environment is taken to be a set of electromagnetic modes in their vacuum state(i.e. unoccupied).

1.2.2 The Master Equation

As the state of a system changes in time, by definition, so will its density matrix. This time evolution is governed by the *master equation*, whose form will depend on the physical processes and approximations involved in a given model. In this dissertation we deal with a master equation of the form

$$\dot{\rho} = -\frac{i}{\hbar}[\hat{H}, \rho] + \frac{1}{2}]\sum_i \gamma_i [2\hat{J}_i \rho \hat{J}_i^\dagger - \hat{J}_i^\dagger \hat{J}_i \rho - \rho \hat{J}_i^\dagger \hat{J}_i], \tag{1.13}$$

where the first term is the *von Neumann equation*[2], and the second is the *Linblad term*[3] [7, 8]. The von Neumann equation describes the time evolution of ρ for a closed system, while the Linblad term accounts for *dissipation* to the environment. Here $\hat{H}$ is the *system* Hamiltonian, and $\hat{J}_i$ is the *jump operator*, or Linblad operator, associated with the i^{th} process involving loss to the environment, taking place at the rate $\gamma_i > 0$.

1.3 Optical Phase Space

In this section we introduce the idea of optical phase space - the description of a system in terms of coherent states. We begin by defining the number states, and use these to motivate the introduction of the creation and annihilation operators, and in turn the coherent states. Section 1.3.6 then describes some of the common representations of optical phase space, including the positive-P representation, which is primarily used in this dissertation.

1.3.1 Number States

Generally $|\psi\rangle$ describes the state of a single particle, in which case we then describe a multi-particle system by giving the state of each particle in an extended Hilbert space. For example, $|\psi_1\rangle \otimes |\psi_2\rangle$ could describe the state of a two-particle system. Unfortunately, for reasons I will not go into, when dealing with indistinguishable particles, this rapidly becomes complicated as the number of particles and states increases.

[2] See Appendix C.1 for a derivation.

[3] There are three key approximations that lead to the derivation of the Linblad form - the Born, Markov, and rotating wave approximations. I will not present a derivation in this text, but an in depth explanation of these approximations can be found in Andrew Daley's review article [7].

Instead of labelling the state of each individual particle, an alternative approach is to state how many particles are in each single-particle state. Quite generally, we would write the state of a multi-particle system as

$$|n_1, n_2, \ldots, n_i, \ldots\rangle\,, \tag{1.14}$$

where n_i is the number of particles in the i^{th} single-particle state.

1.3.2 Creation and Annihilation Operators

The creation operator, $\hat{a}_i^\dagger$, and its adjoint, the annihilation operator, $\hat{a}_i$, are defined in terms of the number states such that

$$\hat{a}_i^\dagger\,|n_1, n_2, \ldots, n_i, \ldots\rangle = \sqrt{n_i+1}\,|n_1, n_2, \ldots, n_i+1, \ldots\rangle\,, \tag{1.15}$$

$$\hat{a}_i\,|n_1, n_2, \ldots, n_i, \ldots\rangle = \sqrt{n_i}\,|n_1, n_2, \ldots, n_i-1, \ldots\rangle\,, \tag{1.16}$$

which is to say they create or destroy a particle in the i^{th} single-particle state. Additionally, the *number operator*, defined as

$$\hat{n}_i = \hat{a}_i^\dagger \hat{a}_i, \tag{1.17}$$

tells us the number of particles in the i^{th} single-particle state:

$$\hat{n}_i\,|n_1, n_2, \ldots, n_i, \ldots\rangle = n_i\,|n_1, n_2, \ldots, n_i, \ldots\rangle\,, \tag{1.18}$$

which can be seen directly from the definitions (1.15) and (1.16).

The commutation relations obeyed by the creation and annihilation operators depends on the quantum statistics obeyed by the particles corresponding to the states they are acting on[4]. In this dissertation we deal exclusively with photons, which are bosons, so we have

$$[\hat{a}_i^\dagger, \hat{a}_j^\dagger] = [\hat{a}_i, \hat{a}_j] = 0, \qquad\qquad [\hat{a}_i, \hat{a}_j^\dagger] = \delta_{ij}, \tag{1.19}$$

where $[A, B] = AB - BA$ is the *commutator*. I will drop the subscript indices as I am only dealing with two distinct single-particle states. It is instead easier to identify them by different letters, i.e. $\hat{a}$ and $\hat{b}$.

1.3.3 Coherent States

The coherent states, $|\alpha\rangle$, are the eigenstates of the annihilation operator, which is to say

$$\hat{a}\,|\alpha\rangle = \alpha\,|\alpha\rangle\,, \tag{1.20}$$

where the eigenvalue α can take on any value in the *complex* plane[5], and is often called the *amplitude* of $|\alpha\rangle$. With respect to the number states, they are defined as[6]

$$|\alpha\rangle = e^{-|\alpha|^2/2} \sum_{n=0}^{\infty} \frac{\alpha^n}{\sqrt{n!}}\,|n\rangle\,. \tag{1.21}$$

Some key properties relevant to this dissertation are:

[4] The many-particle wave function of a bosonic system must be symmetric (under particle exchange), while a fermionic system must be antisymmetric.

[5] The eigenvalues of a Hermitian operator must be real-valued, but the annihilation operator is, by definition, not Hermitian because its adjoint is the creation operator.

[6] See Appendix C.2 for a derivation.

1. The coherent states are *not orthogonal*, which can be shown directly from (1.21):

$$\langle\alpha|\beta\rangle = e^{\alpha^*\beta - |\alpha|^2/2 - |\beta|^2/2} \neq \delta(\alpha - \beta). \tag{1.22}$$

When α and β are far apart this approaches 0, but when they are close to each other there is significant overlap between states. We do still have the *normalisation* $\langle\alpha|\alpha\rangle = 1$, which can be verified by setting $\beta = \alpha$ in (1.22). To illustrate the overlap of coherent states, note that the probability distribution of a coherent state in terms of number states is *Poissonian:*

$$|\langle n|\alpha\rangle|^2 = \left|\langle n| e^{-|\alpha|^2/2} \sum_m \frac{\alpha^m}{\sqrt{m!}} |m\rangle\right|^2 = \left|e^{-|\alpha|^2/2} \frac{\alpha^n}{\sqrt{n!}}\right|^2 = e^{-|\alpha|^2} \frac{|\alpha|^{2n}}{n!} = e^{-\langle n\rangle} \frac{\langle n\rangle^n}{n!}. \tag{1.23}$$

2. The coherent states form a *complete* basis; they are described as being *over complete* due to their lack of orthogonality.

3. The identity in the coherent state basis is given without derivation as

$$\mathbb{1} = \frac{1}{\pi} \int d^2\alpha\, |\alpha\rangle\langle\alpha|\,, \tag{1.24}$$

where $d^2\alpha$ indicates an integral over the complex plane. This has a form similar to that of the usual identity (1.7) for an orthonormal, complete basis, but is scaled by π due to the over-completeness of the coherent states.

4. The eigenvalue α can be interpreted as the *expectation value* of the annihilation operator,

$$\langle\hat{a}\rangle_\alpha = \langle\alpha|\hat{a}|\alpha\rangle = \langle\alpha|\alpha|\alpha\rangle = \alpha, \tag{1.25}$$

although it is often more relevant to consider the expectation value of the *number of particles*,

$$\langle\hat{n}\rangle_\alpha = \langle\hat{a}^\dagger\hat{a}\rangle_\alpha = |\alpha|^2. \tag{1.26}$$

1.3.4 Action of Creation & Annihilation Operators

For completeness, the action of the creation and annihilation operators on the coherent state kets and bras are [9][7]

$$\hat{a}\,|\alpha\rangle = \alpha\,|\alpha\rangle\,, \tag{1.27}$$

$$\hat{a}^\dagger\,|\alpha\rangle = \left(\frac{\alpha^*}{2} + \frac{\partial}{\partial\alpha}\right)|\alpha\rangle\,, \tag{1.28}$$

$$\langle\alpha|\,\hat{a}^\dagger = \langle\alpha|\,\alpha^*, \tag{1.29}$$

$$\langle\alpha|\,\hat{a} = \left(\frac{\alpha}{2} + \frac{\partial}{\partial\alpha^*}\right)\langle\alpha|\,. \tag{1.30}$$

(1.27) is redundant as it was used to define the coherent states, and (1.29) is also trivial since the creation operator is the adjoint of the annihilation operator. The other two equations can be shown from the definition (1.21). As an example, (1.28) is derived in Appendix C.3. The important point to note is that the action of the creation and annihilation operators on coherent kets and bras can be written in terms of *differential operators* with respect to the coherent amplitude α. These will be useful when determining operator correspondences in Section 1.3.7.

[7] These are also presented in [9], although slightly incorrect as the factor of $\frac{1}{2}$ is on the wrong term in (1.28) and (1.30).

1.3.5 Quadrature Operators

Before continuing the discussion of optical phase space, we make a brief aside that will be relevant later in this dissertation. The *quadrature operators* are defined with respect to the creation and annihilation operators as

$$\hat{X} = \hat{a} + \hat{a}^\dagger, \qquad \hat{Y} = i[\hat{a} - \hat{a}^\dagger], \tag{1.31}$$

which satisfy the commutation relation $[\hat{X}, \hat{Y}] = 2i$, and in turn the product of their uncertainties is governed by the Heisenberg uncertainty relation

$$\Delta X \Delta Y \geq 1, \tag{1.32}$$

where ΔX refers to the standard deviation of measurements of $\hat{X}$. It is worth noting that we define these operators because the creation and annihilation operators are not Hermitian, so cannot correspond to physical observables. On the other hand, $\hat{X}$ and $\hat{Y}$ are Hermitian, so can be experimentally measured. They are closely related to the $\hat{x}$ and $\hat{p}$ operators.

When considering the quadrature operators, a system is said to be in a *squeezed state* if one of the operators has a standard deviation less than that of the ground state. Squeezed light has many practical uses such as in the detection of small phase shifts, and in interferometry [9]. The inequality (1.32) is always satisfied, so if the standard deviation of one quadrature operator decreases, the other quadrature operator's will increase. In their ground state (the vacuum), both quadratures have a standard deviation of one, i.e. $\Delta X \Delta Y = \Delta X = \Delta Y = 1$. An important feature of coherent states is that they are also minimum uncertainty states in this sense [10].

1.3.6 Representing the Density Matrix in Phase Space

We now consider how a system can be described in terms of the coherent states - this is referred to as *optical phase space*, but first it is worth noting why we would want to use coherent states rather than, say, number states to describe a system. Quantum optical systems tend to be driven by highly coherent laser fields, which in turn are well described by coherent states. This means that optical phase space methods scale well numerically, which is in contrast to the number states, which do not scale as well for quantum optical systems. As mentioned in Section 1.3.3, the coherent states correspond to a Poissonian distribution of number states. I return to the discussion of phase space versus number states in Chapter 5.

In Section 1.2 I introduced the density matrix, defining it for a discrete set of states in (1.9). The natural generalisation to a continuous set of orthonormal states is

$$\rho = \int dx\, P(x) \left|x\right\rangle\!\left\langle x\right|, \tag{1.33}$$

where $P(x)$ is a probability density function, and acts as a representation of the density matrix in terms of the set of states $\{|x\rangle\}$. This set of states is often taken to be a a set of basis states. It may be tempting to substitute in $|x\rangle = |\alpha\rangle$ and claim that the resulting probability density represents the density matrix in terms of the coherent states, but it is not quite so easy. Instead, the analogue to (1.33) for coherent states is [9]

$$\rho = \int d^2\alpha\, P(\alpha, \alpha^*) \left|\alpha\right\rangle\!\left\langle \alpha\right|, \tag{1.34}$$

where $P(\alpha, \alpha^*)$ cannot be interpreted as a true probability density due to the over-completeness of the coherent states. We call $P(\alpha, \alpha^*)$ the P function, and refer to it as a quasi-probability density. Also note that α is complex-valued, so we integrate over the complex plane. For the same reason, $P(\alpha, \alpha^*)$ is a function of two variables[8]. For completeness, it should be noted that an equivalent definition of the P function is [9]

$$P(\alpha, \alpha^*) = \frac{1}{\pi^2} \int d^2\lambda \; e^{-\lambda\alpha^* + \lambda^*\alpha} \chi_P(\lambda, \lambda^*), \tag{1.35}$$

which is a Fourier transform of the *characteristic function* $\chi_P(\lambda, \lambda^*)$

$$\chi_P(\lambda, \lambda^*) = \mathrm{Tr}\Big[\rho e^{-\lambda\hat{a}^\dagger} e^{\lambda^*\hat{a}}\Big]. \tag{1.36}$$

(1.35) is useful in the sense that it takes on a similar form to two alternative representations of optical phase space - the Q and Wigner functions. These are not used in this dissertation, but it is worth noting that they differ from the P function only by the form of their characteristic functions[9]:

$$\chi_Q(\lambda, \lambda^*) = \mathrm{Tr}\Big[\rho e^{-\lambda^*\hat{a}} e^{\lambda\hat{a}^\dagger}\Big], \qquad \chi_W(\lambda, \lambda^*) = \mathrm{Tr}\Big[\rho e^{-\lambda^*\hat{a} + \lambda\hat{a}^\dagger}\Big]. \tag{1.37}$$

More importantly, the representation of phase space used in this dissertation is the positive-P function, which is a non-diagonal generalisation of the P-function obtained by expanding in terms of two independent sets of coherent states. It is defined as the function $P(\alpha, \alpha^+)$ that satisfies [10]

$$\rho = \int d^2\alpha \, d^2\alpha^+ \, P(\alpha, \alpha^+) \frac{|\alpha\rangle\langle\alpha^{+*}|}{\langle\alpha^{+*}|\alpha\rangle}, \tag{1.38}$$

where the variables α and α^+ are independent. This can be thought of intuitively by considering the analogue for a discrete set of bases, which simply involves inserting the identity into (1.9):

$$\rho = \sum_{\psi} P_\psi \, |\psi\rangle\langle\psi| = \sum_{\psi,\phi} P_\psi \, |\psi\rangle\langle\psi|\phi\rangle\langle\phi| \equiv \sum_{\psi,\phi} \tilde{P}_{\psi,\phi} \, |\psi\rangle\langle\phi| \, . \tag{1.39}$$

All the phase space functions discussed above can be expanded as needed to include multiple variables. For example, in this dissertation we primarily deal with two modes, so use $P(\boldsymbol{\alpha}, \boldsymbol{\alpha}^+)$, where $\boldsymbol{\alpha} = (\alpha, \beta)$ and $\boldsymbol{\alpha}^+ = (\alpha^+, \beta^+)$.

1.3.7 Operator Correspondences of the Positive-P Function

Simply stating a function that represents the density matrix in phase space is not immediately useful. Ultimately we want to turn the time evolution of the system as given by its master equation into an equation for $P(\alpha, \alpha^+)$. The master equation for triplet down conversion is given in Section 1.5, where we see that the only operators involved are the creation and annihilation operators for each mode. This is a common feature of quantum optical systems, so it is natural to ask "if the

[8] It may appear unusual that we define a function in terms of α and its conjugate, but this is equivalent to defining $\mathfrak{Re}[\alpha]$ and $\mathfrak{Im}[\alpha]$ individually. We write it in this form because both α and α^* appear explicitly in the definition of $P(\alpha, \alpha^*)$ in (1.35).

[9] Note that when dealing with non-commuting operators in exponents, their order matters - so χ_P, χ_Q, and χ_W are all different.

creation or annihilation operator acts on the density matrix, what is the corresponding function in phase space?" These *operator correspondences* for the positive-P function are[10] [10]

$$\hat{a}\rho \longleftrightarrow \alpha\, P(\alpha, \alpha^+), \tag{1.40}$$

$$\hat{a}^\dagger \rho \longleftrightarrow \left(\alpha^+ - \frac{\partial}{\partial \alpha}\right) P(\alpha, \alpha^+), \tag{1.41}$$

$$\rho\hat{a} \longleftrightarrow \left(\alpha - \frac{\partial}{\partial \alpha^+}\right) P(\alpha, \alpha^+), \tag{1.42}$$

$$\rho\hat{a}^\dagger \longleftrightarrow \alpha^+ P(\alpha, \alpha^+), \tag{1.43}$$

which can be derived by applying the operator actions (1.27) - (1.30) to the density matrix in the form (1.38). As an example, (1.41) is derived in Appendix C.4. The important point is that in phase space the master equation takes the form of a partial differential equation (PDE). Due to the partial nature of the derivatives, these correspondences are easily expanded to more variables. Before discussing exactly how these correspondences are used in practice to model the time evolution of systems in optical phase space, I will introduce some important ideas about stochastic processes.

1.4 Stochastic Processes

A stochastic process is one which describes a system whose time evolution is not deterministic, but is rather governed by probability laws. They play a vital role in this project because ultimately the mapping into optical phase space results in equations of motion containing stochastic terms, as will be discussed in Section 1.4.6. There are two over-arching ways to describe stochastic processes: we can develop equations of motion for either the trajectory of a single path in stochastic motion - often called a *sample path*, or for the probability distribution that describes the trajectories of all paths [9].

The simplest form of non-trivial stochastic processes is a *Markov process*, in which the future time evolution of a system is determined by its *current* state, and not affected by its state at any previous time [9]. This accurately models most physical stochastic processes. When considering Markov processes, the equations of motion used to describe a sample path are called *stochastic differential equations*[11] (SDEs), whereas the equations of motion for probability distributions are called *Fokker-Planck equations* (FPEs)[12].

1.4.1 Measurements of a Fluctuating System

The mean of a stochastic variable $x(t)$, denoted by an over-bar, $\overline{x(t)}$, is the mean of $x(t)$ at time t. The notation $\langle x(t)\rangle$ is reserved for quantum expectation values. Multivariate systems are represented as vector-valued variables, $\mathbf{x}(t)$, with $\overline{\mathbf{x}(t)}$ a corresponding vector containing the mean of each variable. The *variance* of $x(t)$,

$$\mathrm{V}[x(t)] = \overline{x(t)x^*(t)} - \overline{x(t)}\;\overline{x^*(t)}, \tag{1.44}$$

[10] More correspondences exist, and further more can be derived from those given, but ultimately they are unimportant to this dissertation. Similar correspondences can be derived for the Q and Wigner functions.

[11] They are also called Langevin equations in certain physical contexts.

[12] A Fokker-Planck equation only describes *continuous* processes, whereas non-continuous stochastic motion is described more generally by a *master equation*. The master equations discussed in Section 1.2.2 are the quantum mechanical generalisation of a master equation in this context [9].

measures the spread of x at the time t. The *standard deviation* is the square root of the variance. Generalising to two variables, we define the *covariance*:

$$\mathrm{C}[x(t_1), y(t_2)] = \overline{x(t_1)y^*(t_2)} - \overline{x(t_1)}\;\overline{y^*(t_2)}. \tag{1.45}$$

It gives a measure of the correlation between $x(t)$ at the time t_1 to the $y(t)$ at the time t_2. A true *correlation* however is normalised to between ± 1 via division by the standard deviation of each variable. It is common to take $x = y$ in order to consider the covariance of x with itself at different times. In the case of a multivariate system, we can consider the covariance between each pair of variables as the elements of a matrix. The diagonal elements are the variances, while the off-diagonal elements are explicitly covariances.

Stationary Processes and the Spectrum: A stationary process is one in which all correlations depend only on time differences. In particular, the covariance becomes a function of only $\tau = t_2 - t_1$. In this case, the Fourier transform of the covariance matrix, referred to as the *Spectrum*, is well defined. The spectrum is often more convenient to work with than the covariance as a function of time. Many stochastic systems approximately reach stationary states once transient time evolution has died out.

1.4.2 Random Variables

A random variable, $\xi(t)$, is formally thought of as one whose value at each time is selected randomly from some ensemble. We take $\xi(t)$ to have an average value of 0, and to be completely independent from any other random variables, or itself at any other time:

$$\overline{\xi(t)} = 0, \qquad\qquad \overline{\xi_i(t)\xi_j(t')} = \delta_{ij}\delta(t - t'). \tag{1.46}$$

The Dirac delta in (1.46) may appear unusual or even pathological, but formally $\xi(t)$ is only defined within an integral, such as in the definition of the Wiener increment (1.50) below.

1.4.3 Stochastic Differential Equations

A SDE for the variable $x(t)$ can be written in the "Langevin" form as [11]

$$\frac{dx}{dt} = a[x(t), t] + b[x(t), t]\,\xi(t), \tag{1.47}$$

where $\xi(t)$ is a random variable subject to (1.46). We say that a corresponds to a *drift process*, while b corresponds to a *diffusion process*. This form appears to be extremely general, but it is shown in [9] that it does in fact meet the requirements of a Markov process. A SDE can also be written in "Itô form" as [11]

$$dx(t) = a[x(t), t]dt + b[x(t), t]dW(t), \tag{1.48}$$

which is mathematical short hand for the integral equation

$$x(t) - x(t_0) = \int_{t_0}^{t} a[x(t'), t']dt' + \int_{t_0}^{t} b[x(t'), t']dW(t'). \tag{1.49}$$

The *Wiener increment*, $dW(t)$, is formally defined by

$$W(t) = \int_0^t \xi(t')dt' \quad \longrightarrow \quad dW(t) = \int_t^{t+dt} \xi(t')dt', \tag{1.50}$$

but can often be thought of as $dW = \xi(t)dt$. From the definition of $\xi(t)$ in Section 1.4.2, we see that $\overline{dW(t)} = 0$, and $\overline{dW(t)^2} = dt$ [11], which is to say that the Wiener increment is Gaussian with a mean of zero and variance of dt. Further specifics of Itô calculus are beyond the scope of this dissertation.

1.4.4 Fokker-Planck Equations

If the motion of a single trajectory of the stochastic variable $x(t)$ is governed by (1.49), then the time evolution of $p(x,t)$ the probability distribution of $x(t)$, is given by the Fokker-Planck equation, which is a PDE of the form [11]

$$\frac{\partial\, p[x(t),t]}{\partial t} = -\frac{\partial}{\partial x}\Big[a[x(t),t]\, p[x(t),t]\Big] + \frac{1}{2}\frac{\partial^2}{\partial x^2}\Big[b[x(t),t]^2\, p[x(t),t]\Big], \tag{1.51}$$

where $a[x(t),t]$ and $b[x(t),t]$ are the same as those given in (1.47). A proof of this relationship is beyond the scope of this dissertation. The important point to note is that a Fokker-Planck equation only contains first and second order derivatives.

1.4.5 Multivariate Systems

An $n-$dimensional multivariate system of SDEs can be written in Itô form as the matrix equation

$$d\mathbf{x} = \mathbf{A}[\mathbf{x}(t),t]dt + B[\mathbf{x}(t),t]d\mathbf{W}(t), \tag{1.52}$$

where $\mathbf{A}$ is the *drift vector*, $BB^T \equiv D$ is the *diffusion matrix*, and $d\mathbf{W}(t)$ is a column vector of independent Wiener increments[13]. The corresponding multivariate FPE is [11]

$$\frac{\partial\, p[x(t),t]}{\partial t} = -\sum_i \frac{\partial}{\partial x_i}\Big[A_i[\mathbf{x}(t),t]\, p[\mathbf{x}(t),t]\Big] + \frac{1}{2}\sum_{i,j}\Big[\frac{\partial^2}{\partial x_i \partial x_j} D_{ij}[\mathbf{x}(t),t]\, p[\mathbf{x}(t),t]\Big] \tag{1.53}$$

where A_i and $[BB^T]_{ij} \equiv D_{ij}$ are elements of the drift vector and diffusion matrix respectively.

1.4.6 The Role of SDEs in Optical Phase Space

The operator correspondences presented in Section 1.3.7 make it clear that a master equation in the form of (1.13) will be mapped to a PDE for $P(\alpha,\alpha^+)$ in phase space. This equation can contain first, second, and potentially higher order derivatives with respect to the phase space variables α and α^+. The usual process is to interpret this as a Fokker-Planck equation, but this can be problematic because a FPE only contains first and second order derivatives. If higher order derivatives exist they must be *truncated* in order to make the mapping to an FPE. If this is required it unfortunately leads to an incomplete description of the physical process in phase space. For the master equation

[13] $d\mathbf{W}(t)$ is not necessarily n-dimensional. For example, in Chapter 4 we will deal with a multivariate SDE which has more Wiener increments than variables.

I am dealing with - which will be given in (1.56) - third order derivatives *do* exist, due to third order operator products in the master equation, so truncation is required.

The resulting FPE is still a partial differential equation which can be difficult to solve analytically or numerically. The usual procedure is to map the FPE to a corresponding SDE [6] via the relationship between their drift and diffusion terms given in Section 1.4.5 for the multivariate case. Solving the resulting SDE will provide solutions for the phase space variables. Averaging these over a large number of trajectories of the SDE will recover the true averages described by the FPE. In turn this recovers the time evolution of the system governed by the master equation the FPE was derived from, albeit with the possibility of discrepancies due to truncation.

1.5 Triplet Down Conversion

We have now introduced the background necessary for the development of the equations of motion for triplet down conversion. The focus of this section is to introduce the master equation that will model the process, and from this develop a set of (truncated) positive-P SDEs.

As stated earlier, triplet down conversion refers to the process of splitting one photon into three. Conservation of energy requires that the frequencies of the generated photons add to that of the original photon. The simplest case to consider is that of triply-degenerate down conversion, in which the generated photons all have frequency one third that of the original photon. The key processes involved are shown schematically in Figure 1.1, and discussed in depth below.

The degenerate interaction Hamiltonian is given by [1]

$$\hat{H}_{\text{int}} = i\hbar\frac{\kappa}{3}\left[\hat{a}^{\dagger 3}\hat{b} - \hat{a}^{3}\hat{b}^{\dagger}\right], \tag{1.54}$$

where κ is the effective non-linearity of the medium in which the process is occurring, which gives a measure of the strength of the interaction. Technically κ should be complex valued, but we exploit our freedom over the overall phase and take it to be real. $\hat{b}^{\dagger}$, $\hat{b}$ are the bosonic creation and annihilation operators for the high energy photons, and $\hat{a}^{\dagger}$, $\hat{a}$ are the corresponding operators for the lower energy mode. The $\hat{a}^{\dagger 3}\hat{b}$ term corresponds to down-conversion - the destruction of one high energy photon, and the creation of three low energy photons, while the $\hat{a}^{3}\hat{b}^{\dagger}$ term corresponds to the reverse process of *third harmonic generation*.

The interaction Hamiltonian on its own does not fully describe the physical process when it takes place inside an optical cavity, as we need to account for interactions with the environment. The two processes to include are i) the introduction of photons to the cavity via pumping, and ii) the spontaneous loss of photons to the environment. The pumping is accounted for via the inclusion of the additional Hamiltonian

$$\hat{H}_{\text{pump}} = i\hbar\left[\epsilon_b\hat{b}^{\dagger} - \epsilon_b^{*}\hat{b}\right], \tag{1.55}$$

where ϵ_b represents the strength of the pumping of the high energy photons. It should be thought of as the classical limit (i.e. many photons) of the annihilation of a photon outside the cavity and the creation of a b photon inside the cavity. This allows it to be included as a *system* Hamiltonian, even though it is the interaction between the system and the environment. (1.55) only supplies photons to the high energy mode, but an analogous Hamiltonian could be included if the low energy mode was also being pumped. In experiments the low energy mode often *will* be pumped in order to seed the interaction, but I will not consider that here - although pumping is reintroduced to

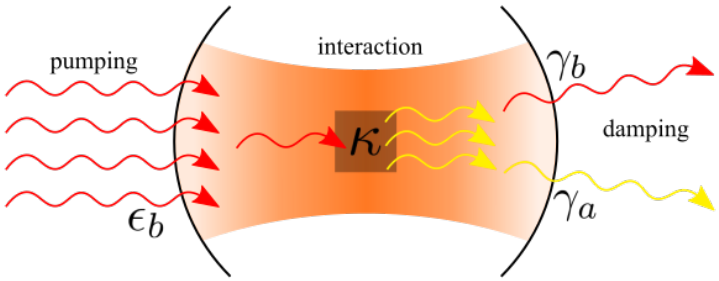

Figure 1.1: The key physical processes that must be included in a model of triplet down conversion within a cavity are the strength of the interaction, the phase and strength of the pumping, and the damping rates for each mode. An optical cavity is chosen such that i) it can sustain both high and low energy modes, and ii) it contains a crystal with a non-linearity that allows for down conversion of photons. Supply of photons to the high energy mode from outside the cavity is modelled in the classical limit of many photons via the c-number ϵ_b, while loss of photons to the environment is described by the damping rates γ_a and γ_b.

the low energy mode in Section 2.2 for a different reason. Additionally, note that in this model the only difference between third harmonic *generation* and down conversion is which mode has the dominant pumping.

The damping is not represented by a system Hamiltonian, but is rather included via Linblad terms in the master equation. In the context of triplet down conversion, the jump operators discussed in Section 1.2.2 are the creation operators for each mode, so the overall master equation is given by

$$\dot{\rho} = -\frac{i}{\hbar}[\hat{H}_{\rm sys}, \rho] + \frac{\gamma_a}{2}[2\hat{a}\rho\hat{a}^\dagger - \hat{a}^\dagger\hat{a}\rho - \rho\hat{a}^\dagger\hat{a}] + \frac{\gamma_b}{2}[2\hat{b}\rho\hat{b}^\dagger - \hat{b}^\dagger\hat{b}\rho - \rho\hat{b}^\dagger\hat{b}], \tag{1.56}$$

where $\hat{H}_{\rm sys} = \hat{H}_{\rm int} + \hat{H}_{\rm pump}$, and γ_a and γ_a are the damping rates of the a and b modes respectively.

In order to map the master equation (1.56) into phase space, we use the positive-P operator correspondences (1.40) - (1.43). In the following derivation I compute the resulting PDEs for terms in the master equation (1.56) corresponding to the interaction, pumping, and damping separately.

1. The portion of the master equation due to the interaction is

$$-\frac{i}{\hbar}[\hat{H}_{\rm int}, \rho] = \frac{\kappa}{3}\left[\hat{a}^{\dagger 3}\hat{b} - \hat{a}^3\hat{b}^\dagger, \rho\right] = \frac{\kappa}{3}\left[\hat{a}^{\dagger 3}\hat{b}\rho - \hat{a}^3\hat{b}^\dagger\rho - \rho\hat{a}^{\dagger 3}\hat{b} + \rho\hat{a}^3\hat{b}^\dagger\right].$$

Applying the operator correspondences (1.40) - (1.43), this is mapped to

$$\frac{\partial P}{\partial t} = \frac{\kappa}{3}\left[\left(\alpha^+ - \frac{\partial}{\partial\alpha}\right)^3\beta - \alpha^3\left(\beta^+ - \frac{\partial}{\partial\beta}\right) - \alpha^{+3}\left(\beta - \frac{\partial}{\partial\beta^+}\right) + \left(\alpha - \frac{\partial}{\partial\alpha^+}\right)^3\beta^+\right]P(\alpha,\alpha^+,\beta,\beta^+).$$

Expanding brackets yields

$$\begin{aligned}\frac{\partial P}{\partial t} = \frac{\kappa}{3}\Bigg[&\cancel{\alpha^{+3}\beta} - 3\alpha^{+2}\frac{\partial}{\partial\alpha}\beta + 3\alpha^+\frac{\partial^2}{\partial\alpha^2}\beta - \frac{\partial^3}{\partial\alpha^3}\beta - \cancel{\alpha^3\beta^+} + \alpha^3\frac{\partial}{\partial\beta}\\ &- \cancel{\alpha^{+3}\beta} + \alpha^{+3}\frac{\partial}{\partial\beta} + \cancel{\alpha^3\beta^+} - 3\alpha^2\frac{\partial}{\partial\alpha^+}\beta^+ + 3\alpha\frac{\partial^2}{\partial\alpha^{+2}}\beta^+ - \frac{\partial^3}{\partial\alpha^{+3}}\beta^+\Bigg]P(\alpha,\alpha^+,\beta,\beta^+),\end{aligned}$$

which can be regrouped in terms of the order of the derivative in each term:

$$\frac{\partial P}{\partial t} = -\left[\frac{\partial}{\partial\alpha}(\kappa\alpha^{+2}\beta) + \frac{\partial}{\partial\alpha^{+}}(\kappa\alpha^{2}\beta^{+}) + \frac{\partial}{\partial\beta}\left(-\frac{\kappa}{3}\alpha^{3}\right) + \frac{\partial}{\partial\beta^{+}}\left(-\frac{\kappa}{3}\alpha^{+3}\right)\right]P(\alpha,\alpha^{+},\beta,\beta^{+})$$
$$+\frac{1}{2}\left[\frac{\partial^{2}}{\partial\alpha^{2}}(2\kappa\alpha^{+}\beta) + \frac{\partial^{2}}{\partial\alpha^{+2}}(2\kappa\alpha\beta^{+})\right]P(\alpha,\alpha^{+},\beta,\beta^{+})$$
$$-\frac{1}{3}\left[\frac{\partial^{3}}{\partial\alpha^{3}}(\kappa\beta^{+}) + \frac{\partial^{3}}{\partial\alpha^{+3}}(\kappa\beta)\right]P(\alpha,\alpha^{+},\beta,\beta^{+}).$$

2. The portion of the master equation due to the pumping is

$$-\frac{i}{\hbar}[\hat{H}_{\text{pump}},\rho] = [\epsilon_b\hat{b}^{\dagger} - \epsilon_b^{*}\hat{b},\rho] = \epsilon_b\hat{b}^{\dagger}\rho - \epsilon_b^{*}\hat{b}\rho - \epsilon_b\rho\hat{b}^{\dagger} + \epsilon_b^{*}\rho\hat{b}.$$

Applying the operator correspondences (1.40) - (1.43), this is mapped to

$$\frac{\partial P}{\partial t} = \left[\epsilon_b\left(\beta^{+} - \frac{\partial}{\partial\beta}\right) - \epsilon_b^{*}\beta - \epsilon_b\beta^{+} + \epsilon_b^{*}\left(\beta - \frac{\partial}{\partial\beta^{+}}\right)\right]P(\alpha,\alpha^{+},\beta,\beta^{+}).$$

Cancelling terms we obtain

$$\frac{\partial P}{\partial t} = -\left[\frac{\partial}{\partial\beta}(\epsilon_b) + \frac{\partial}{\partial\beta^{+}}(\epsilon^{*})\right]P(\alpha,\alpha^{+},\beta,\beta^{+}),$$

and analogously for the a mode if it has pumping included.

3. The portion of the master equation due to the damping of the a mode is

$$\gamma_a[2\hat{a}\rho\hat{a}^{\dagger} - \hat{a}^{\dagger}\hat{a}\rho - \rho\hat{a}^{\dagger}\hat{a}].$$

Applying the operator correspondences (1.40) - (1.43), this is mapped to

$$\frac{\partial P}{\partial t} = \gamma_a\left[2\alpha\alpha^{+} - \left(\alpha^{+} - \frac{\partial}{\partial\alpha}\right)\alpha - \left(\alpha - \frac{\partial}{\partial\alpha^{+}}\right)\alpha^{+}\right]P(\alpha,\alpha^{+},\beta,\beta^{+}).$$

Cancelling terms we obtain

$$\frac{\partial P}{\partial t} = -\left[-\frac{\partial}{\partial\alpha}(\gamma_a\alpha) - \frac{\partial}{\partial\alpha^{+}}(\gamma_a\alpha^{+})\right]P(\alpha,\alpha^{+},\beta,\beta^{+}),$$

and analogously for the damping of the b mode.

The overall PDE determining the time evolution of the system in phase space is found by combining these three equations:

$$\begin{aligned}\frac{\partial P}{\partial t} = &-\Bigg[\frac{\partial}{\partial\alpha}(\kappa\alpha^{+2}\beta) + \frac{\partial}{\partial\alpha^+}(\kappa\alpha^2\beta^+) + \frac{\partial}{\partial\beta}\left(-\frac{\kappa}{3}\alpha^3\right) + \frac{\partial}{\partial\beta^+}\left(-\frac{\kappa}{3}\alpha^{+3}\right) \\ &\qquad - \frac{\partial}{\partial\alpha}(\gamma_a\alpha) - \frac{\partial}{\partial\alpha^+}(\gamma_a\alpha^+) + \frac{\partial}{\partial\beta}(\epsilon_b) + \frac{\partial}{\partial\beta^+}(\epsilon_b^*)\Bigg] P(\alpha,\alpha^+,\beta,\beta^+) \\ &+\frac{1}{2}\left[\frac{\partial^2}{\partial\alpha^2}(2\kappa\alpha^+\beta) + \frac{\partial^2}{\partial\alpha^{+2}}(2\kappa\alpha\beta^+)\right] P(\alpha,\alpha^+,\beta,\beta^+) \\ &-\frac{1}{3}\left[\frac{\partial^3}{\partial\alpha^3}(\kappa\beta^+) + \frac{\partial^3}{\partial\alpha^{+3}}(\kappa\beta)\right] P(\alpha,\alpha^+,\beta,\beta^+).\end{aligned} \tag{1.57}$$

The first term contains only first order derivatives, and corresponds to a drift term in a Fokker-Planck equation. Likewise, the second term contains only second order derivative, and corresponds to a diffusion term in a Fokker-Planck equation. The third term contains third order derivatives, so cannot be mapped to a Fokker-Planck equation. Instead we ignore the term by truncating the PDE to second order. A discussion of the validity of this procedure is provided in Chapter 5.

We now have a multivariate Fokker Planck equation of the form (1.53). The results of Section 1.4.5 tell us that the drift vector and diffusion matrix for the system are given respectively as

$$A = \begin{bmatrix} \gamma_a\alpha + \kappa\alpha^{+2}\beta \\ \gamma_a\alpha^+ + \kappa\alpha^2\beta^+ \\ \epsilon_b - \frac{\kappa}{3}\alpha^3 \\ \epsilon_b^* - \frac{\kappa}{3}\alpha^{+3} \end{bmatrix}, \qquad BB^T = D = \begin{bmatrix} 2\kappa\alpha^+\beta & 0 & 0 & 0 \\ 0 & 2\kappa\alpha\beta^+ & 0 & 0 \\ 0 & 0 & 0 & 0 \\ 0 & 0 & 0 & 0 \end{bmatrix}. \tag{1.58}$$

Using the form of a multivariate SDE (1.52), we see that this corresponds to the following set of coupled SDEs for the phase space variables α, α^+, β and β^+:

$$\begin{aligned}\dot{\alpha} &= -\gamma_a\alpha + \kappa\alpha^{+2}\beta + \sqrt{2\kappa\alpha^+\beta}\,\xi_1(t), \\ \dot{\alpha}^+ &= -\gamma_a\alpha^+ + \kappa\alpha^2\beta^+ + \sqrt{2\kappa\alpha\beta^+}\,\xi_2(t), \\ \dot{\beta} &= \epsilon_b - \gamma_b\beta - \frac{\kappa}{3}\alpha^3, \\ \dot{\beta}^+ &= \epsilon_b^* - \gamma_b\beta^+ - \frac{\kappa}{3}\alpha^{+3}.\end{aligned} \tag{1.59}$$

where ξ_1 and ξ_2 are real-valued Gaussian random variables as defined in (1.46). It should be noted that these equations are *truncated*, as discussed in Section 1.4.6. The α and α^+ equations have explicit drift and diffusion terms, while the β and β^+ equations only have drift terms - however, they still undergo stochastic time evolution, but it is included implicitly in the α and α^+ terms.

Computing Moments from the Phase Space Variables: Solving (1.59) will yield solutions for the positive-P phase space variables α, α^+, β and β^+ over time, but these are only related to physically meaningful quantities in the stochastic averages over many trajectories described by (1.59). In the limit of many trajectories we recover the statistics described by the associated Fokker-Planck equation, i.e. $\overline{\alpha^{+m}\alpha^n} \to \langle\alpha^{+m}\alpha^n\rangle$, and the same for the β terms. Additionally, normally

ordered operator moments[14] can be calculated from the positive-P function [12]:

$$\langle \hat{a}^{\dagger m} \hat{a}^n \rangle = \int d^2\alpha \; d^2\alpha^+ \; \alpha^{+m} \alpha^n P(\alpha, \alpha^+) \equiv \left\langle \alpha^{+m} \alpha^n \right\rangle . \tag{1.60}$$

Combining these results, we find that stochastic averages of the phase space variables approach normally ordered operator moments:

$$\overline{\alpha^{+m} \alpha^n} \longrightarrow \langle \hat{a}^{\dagger m} \hat{a}^n \rangle, \qquad \overline{\beta^{+m} \beta^n} \longrightarrow \langle \hat{b}^{\dagger m} \hat{b}^n \rangle. \tag{1.61}$$

In fact, the *only* statistics that simulations of (1.59) can recover are operator moments. Of most interest to my work, and the focus of Chapter 2 are the mode populations $\langle \hat{a}^\dagger \hat{a} \rangle \equiv \langle \hat{n}_a \rangle$ and $\langle \hat{b}^\dagger \hat{b} \rangle \equiv \langle \hat{n}_b \rangle$.

[14] Normally ordered operator products are those in which all creation operators are to the left of all annihilation operators. A moment is the expectation value of the product of operators.

Chapter 2

Time Evolution and Steady States of the Mode Populations

Chapter 1 has covered some vital background information, and introduced the model that will be the focus of this dissertation. This chapter begins the presentation of my work by investigating the time evolution of the mode populations. As outlined in Section 1.5, these are calculated from the stochastic average of individual trajectories of the phase space variables given by the coupled SDEs (1.59). This was achieved by running a Monte Carlo simulation of 20,000 trajectories of (1.59) using the SDE solvers in the `DifferentialEquations.jl` package for Julia. An in depth discussion of the numerics involved is presented in Appendix B, where it is shown that enough trajectories are averaged over in order for the simulations to converge, and that sufficient tolerances were used in the numerical integration.

The simulations were compared to a semi-classical approximation, which involved dropping the stochastic terms from (1.59). The argument for this is that on average the stochastic terms will not significantly influence the overall time evolution, but we will see this is not true. For the semi-classical simulation we make the convenient choice of initial conditions

$$\alpha^{+}(0) = \alpha_0^*, \qquad \beta^{+}(0) = \beta_0^*, \tag{2.1}$$

where $\alpha_0 \equiv \alpha(0)$, and $\beta_0 \equiv \beta(0)$. This is to say that both modes begin in a coherent state. The lack of stochastic terms then fixes $\alpha^{+}(t) = \alpha^{*}(t)$, and the same for β, which reduces (1.59) to just two equations

$$\begin{aligned} \dot{\alpha} &= \kappa \alpha^{*2} \beta - \gamma_a \alpha, \\ \dot{\beta} &= \epsilon_b - \frac{\kappa}{3}\alpha^3 - \gamma_b \beta, \end{aligned} \tag{2.2}$$

with α^{+} and β^{+} being recovered by complex conjugation.

The most physically relevant initial condition would be to begin the system in the vacuum state, i.e. $\alpha(0) = \alpha^{+}(0) = \beta(0) = \beta^{+}(0) = 0$[1]. However, inspection of (1.59) shows that the interaction will not proceed if α and α^{+} are equal to zero[2]. To get around this I considered starting the

[1] Note that this still satisfies (2.1).

[2] This is not physical - it is a result of the truncation discussed in Section 1.3.7. This identifies a limitation of the phase space methods being used.

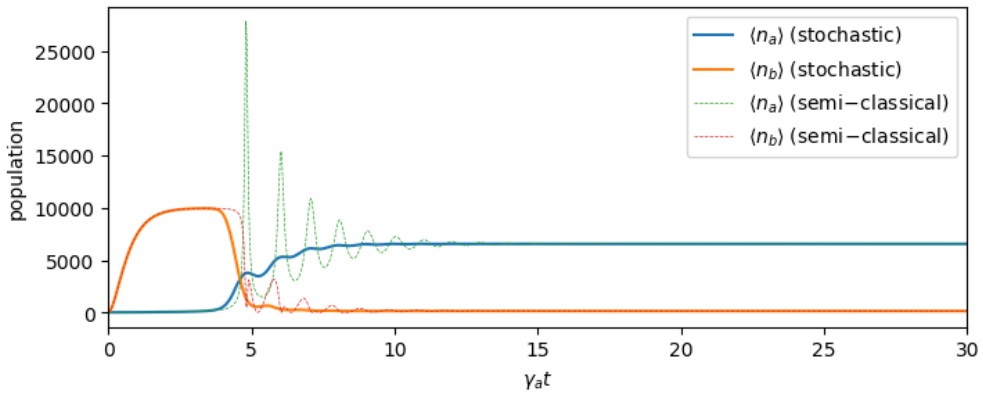

Figure 2.1: Time evolution of the expected mode populations, $\langle n_a \rangle$ and $\langle n_b \rangle$, as given by stochastic integration of the truncated positive-P SDEs (1.59), and by the semi-classical approximation (2.2). The parameters used are $\kappa = 0.001, \gamma_b = 2\gamma_a, \epsilon_a = 5\gamma_a$, and $\epsilon_b = 200\gamma_a$.

system "near" the vacuum, but for the parameters used the damping took α and α^+ to zero before anything interesting happened. Instead, I implemented the work around used in [1], in which a weak "seed" pump, ϵ_a, is used to drive the a mode. As long as ϵ_a is relatively small compared to ϵ_b, this shouldn't affect the overall nature of the time evolution significantly, which is confirmed in Section 2.2.

Throughout this dissertation we take $\gamma_a = 1$ (except briefly in section 2.3.1), which provides a characteristic time scale for all parameters and simulations. In Sections 2.1 and 2.2 the parameters $\kappa = 0.001, \gamma_b = 2\gamma_a, \epsilon_a = 5\gamma_a$, and $\epsilon_b = 200\gamma_a$ are used. They are physically reasonable values that satisfy $\epsilon_a \ll \epsilon_b$. I begin by comparing the time evolution of the mode populations as given by full stochastic integration of (1.59) to that of the semi-classical coupled ODEs (2.2). I then investigate techniques for removing the pumping of the a mode once the interaction has begun, which is desirable for physically relevant results. Finally, the majority of this chapter focuses on the effect of ϵ_b on the time evolution. An emphasis is placed on these, as they provide the results required for further analysis in Chapter 3.

2.1 Comparison of Stochastic & Semi-Classical Results

The time evolution of $\langle n_a \rangle$ and $\langle n_b \rangle$ as given by both the truncated positive-P and semi-classical simulations are presented in Figure 2.1. Broadly speaking, the two simulations exhibit consistent behaviour: as photons are supplied to the b mode, the number of high energy photons increases rapidly, then reaches a fairly steady number as the damping balances it out. At some critical point the down conversion of photons increases rapidly, leading to a decrease in high energy photons and an increase in low energy photons. The exact behaviour at this point differs between the techniques, but they both agree that a *steady state* is eventually reached - which is to say $\langle n_a \rangle$ and $\langle n_b \rangle$ are constant in time - and agree on the steady state populations for both modes.

To understand why the semi-classical approximation greatly exaggerates the magnitude of the oscillatory transient behaviour, it is important to note that individual trajectories of the stochastic simulation behave similarly to the semi-classical simulation. The key difference is that the oscillations are shifted slightly forward or back in time, as shown in Figure 2.2. It appears that the

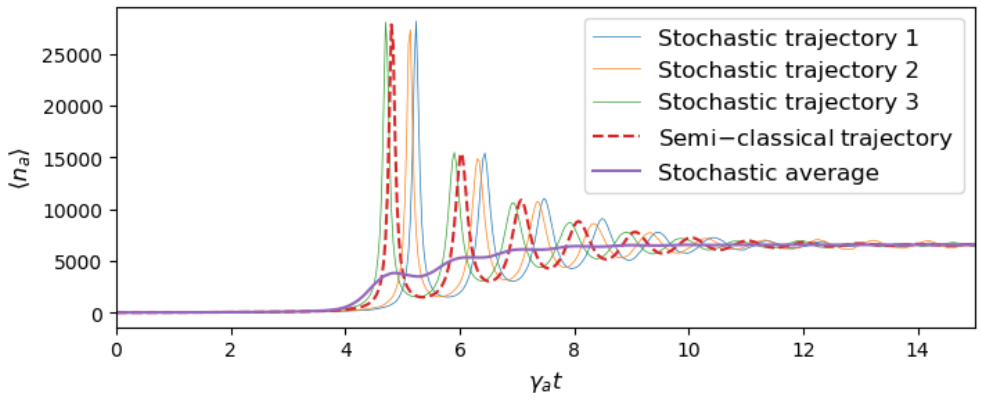

Figure 2.2: The time evolution of $\langle n_a \rangle$ until $\gamma_a t = 15$ for three individual trajectories of the truncated positive-P SDEs (1.59), with comparison to the stochastic average of 20,000 trajectories, and the solution to the semi-classical approximation (2.2). The parameters used are $\kappa = 0.001, \gamma_b = 2\gamma_a, \epsilon_a = 5\gamma_a$, and $\epsilon_b = 200\gamma_a$.

semi-classical approximation is valid except around the critical point that leads to rapid growth of $\langle n_a \rangle$ - i.e. the stochastic terms are large enough to noticeably affect when the system reaches this critical point. It is typical for quantum effects to be most evident near a critical point like this.

2.2 Removing Pumping from the Low Energy Mode

The results presented in Figure 2.1 correspond to a system which has photons supplied to the low energy mode, albeit significantly slower than the high energy mode. This pumping was introduced because a system governed by (1.59) will not produce down converted photons without some pumping of the low energy mode. This is a result of the truncation involved in deriving (1.59), so should not be interpreted as a physical requirement. It is desirable compare the steady states obtained in section 2.1 with those corresponding to $\epsilon_a = 0$. There are two techniques that can be used to achieve this:

1. The first is to run a simulation with the inclusion of $\epsilon_a \neq 0$, then set it equal to zero once the steady state has been reached. This is easily achieved via the inclusion of an `if` statement when defining the SDE. For the results presented in this section the pumping is turned off at $t = 15$.

2. The second is to begin the simulation with $\epsilon_a = 0$, but in an initial state well away from the vacuum. This technique was not implemented in Section 2.1 because the time evolution from the vacuum was desired. If the quantities of interest only involve the steady state - which tends to be the case in experiments, the exact time evolution is unimportant, and this technique is valid. For the results presented in this section, the initial values $\alpha, \alpha^+ = 60$ were used.

The time evolution of systems implementing both of these techniques are compared to the results from Section 2.1 in Figure 2.3. The two techniques yield consistent results in the steady state, and unsurprisingly the steady state value of $\langle n_a \rangle$ is slightly less than when the a mode is pumped.

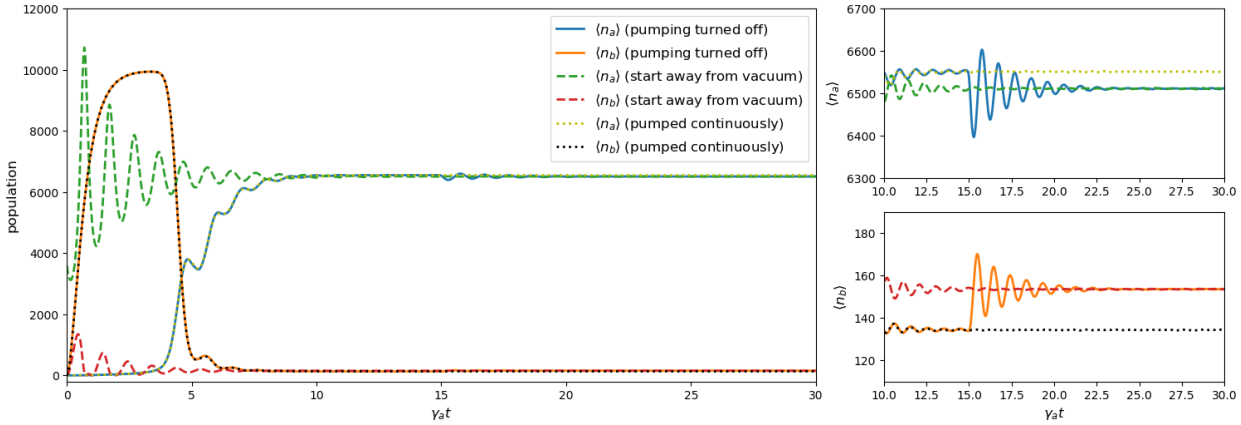

Figure 2.3: The time evolution of $\langle n_a \rangle$ and $\langle n_b \rangle$ when the a mode is pumped compared to two methods used to set $\epsilon_a = 0$ in the steady state. The parameters used are $\kappa = 0.001, \gamma_b = 2\gamma_a, \epsilon_b = 200\gamma_a$, and $\epsilon_a = 5\gamma_a$ and 0 respectively.

Correspondingly, the steady state value of $\langle n_b \rangle$ is slightly larger. The similarity between the two steady states is encouraging as it indicates that the inclusion of $\epsilon_a \neq 0$ did not significantly affect the time evolution. This has been further confirmed by setting $\epsilon_a = 0$ at earlier times: for any time after $\gamma_a t \approx 5$ the time evolution proceeds almost identically (earlier than this the damping is dominant and takes $\langle n_a \rangle$ to zero).

2.3 Effect of Pumping of the High Energy Mode

Sections 2.1 and 2.2 have presented results pertaining to the single set of parameters $\kappa = 0.001, \gamma_b = 2\gamma_a$, and $\epsilon_b = 200\gamma_a$, with $\epsilon_a = 0$ or $5\gamma_a$. In order to get a better understanding of the system we now consider the effect of ϵ_b on the time evolution, and the steady states in particular.

2.3.1 Over-Damped Regime

I begin by considering a completely new set of parameters, which has been used elsewhere in the literature [2]: $\kappa = 1, \gamma_a = 0.1, \gamma_b = 10$ and $\epsilon_a = 0$. I refer to this as the "over-damped" regime because it satisfies the condition $\gamma_b \gg \gamma_a$. Ideally I would determine the steady states of this system as a function of ϵ_b by running stochastic simulations of (1.59), but this was found to be unstable for these parameters. However, in Section 2.1, it was shown that the steady states of the ODE are consistent with the full SDE. Whether this is true for all ϵ_b is addressed in Section 2.3.2, but for now I will deal with the semi-classical coupled ODEs (2.2). Working in the over-damped regime allows for the development of an analytic relationship between the pumping and the steady states of (2.2). These are compared to numerical results obtained i) using a steady state solver available in `DifferentialEquations.jl`, and ii) by running simulations of (2.2). In Section 2.3.2 we will return to the parameters used in Sections 2.1 and 2.2. The analytic result is not valid in this case, but the numerical results can still be obtained and will be compared to steady states obtained from simulations of the coupled SDEs (1.59).

Analytic Solution

To begin, I solve for the steady states of the ODE analytically. In order to do this I will restrict myself to the situation in which the damping of the high energy mode is much greater than that of the low energy mode, i.e. $\gamma_b \gg \gamma_a$. This means that the b mode evolves on a much shorter time scale than the a mode, so as a result of the adiabatic approximation [13] we can solve for the steady state of the a mode, knowing that the b mode will be slaved to it. This is referred to as *adiabatic elimination* of the a mode. So we begin by setting $\dot{\alpha} = 0$, allowing us to determine the steady state condition on β:

$$\dot{\alpha} = \epsilon_b - \frac{\kappa}{3}\alpha^3 - \gamma_b\beta_s = 0 \quad \Longrightarrow \quad \beta_s = \frac{\epsilon_b - \kappa/3\ \alpha_s^3}{\gamma_b}, \tag{2.3}$$

where a subscript s denotes a steady state. We can substitute this back into (2.2) in order to determine a steady state condition on α alone:

$$\frac{\kappa\alpha_s^{*2}[\epsilon_b - \kappa/3\ \alpha_s^3]}{\gamma_b} - \gamma_a\alpha_s = 0. \tag{2.4}$$

Note that (2.4) implicitly includes (2.3), the steady state condition on β. We proceed by explicitly writing $\alpha_s = |\alpha_s|e^{i\theta}$ in order to split (2.4) into its phase and magnitude components:

$$\begin{aligned}
\frac{\kappa|\alpha_s|^2e^{-i2\theta}[\epsilon_b - \kappa/3|\alpha_s|^3e^{i3\theta}]}{\gamma_b} - \gamma_a|\alpha_s|e^{i\theta} &= 0, \\
\frac{\kappa\epsilon_b}{\gamma_b}|\alpha_s|^2e^{-i2\theta} - \frac{\kappa^2}{3\gamma_b}|\alpha_s|^5e^{i\theta} - \gamma_a|\alpha_s|e^{i\theta} &= 0, \\
|\alpha_s|\left[\frac{\kappa\epsilon_b}{\gamma_b}|\alpha_s|e^{-i3\theta} - \frac{\kappa^2}{3\gamma_b}|\alpha_s|^4 - \gamma_a\right] &= 0.
\end{aligned}$$

This has factorised the solutions for $|\alpha_s|$ into two sets:

1. There is an obvious *trivial solution*,

$$\alpha_s = 0. \tag{2.5}$$

   The corresponding solution for the b mode is found from (2.3) to be $\beta_s = \frac{\epsilon}{\gamma_b}$.

2. Of more interest are the *non-trivial solutions*, found by solving the quartic

$$\frac{\kappa\epsilon_b}{\gamma_b}|\alpha_s|e^{-i3\theta} - \frac{\kappa^2}{3\gamma_b}|\alpha_s|^4 - \gamma_a = 0, \tag{2.6}$$

   of which I will consider the phase and magnitude separately. Note that because κ, γ_a and γ_b are all real and positive, the last two terms lie along the negative real axis. So in order to satisfy the equation, the first term must lie along the positive real axis, i.e.

$$\frac{\kappa\epsilon_b}{\gamma_b}|\alpha_s|e^{-i3\theta} = \frac{\epsilon_b}{|\epsilon_b|}\frac{\kappa|\epsilon_b|}{\gamma_b}|\alpha_s|e^{-i3\theta} \qquad \text{is real and positive.} \tag{2.7}$$

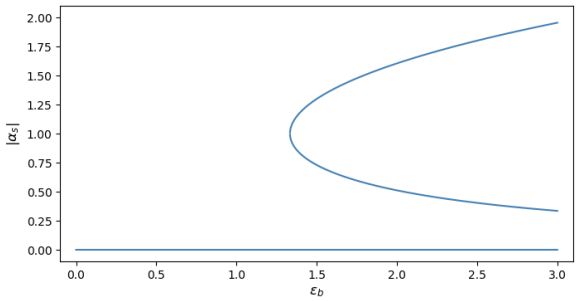

(a) Analytic result given by (2.5) and (2.9)

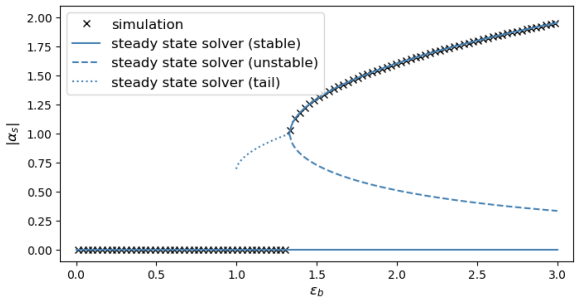

(b) Numerical results given by the steady state solver, and from simulations of (2.2)

Figure 2.4: The steady state values of $|\alpha|$ as a function of the pump intensity ϵ_b. The dashed lines indicate *unstable* solutions, and the dotted "tail" is not a true steady state. The non-trivial solutions begin at $\epsilon_b = 4/3$. The parameters used are $\kappa = 1$, $\gamma_a = 0.1, \gamma_b = 10$ and $\epsilon_a = 0$ (satisfying $\gamma_a \ll \gamma_b$).

I have introduced the factor of $\frac{|\epsilon_b|}{|\epsilon_b|} = 1$ because $\frac{\epsilon_b}{|\epsilon_b|}$ has unit magnitude while $\frac{\kappa|\epsilon_b|}{\gamma_b}$ has no phase. In terms of phase I can therefore write

$$\frac{\epsilon_b}{|\epsilon_b|}e^{-i3\theta} = 1 \implies \boxed{e^{i3\theta} = \frac{\epsilon_b}{|\epsilon_b|} \equiv \arg(\epsilon_b),} \tag{2.8}$$

which specifies 3 solutions for θ. We can substitute this result back into (2.6) and solve for the magnitude of α_s:

$$\frac{\kappa|\epsilon_b|}{\gamma_b}|\alpha_s| - \frac{\kappa^2}{3\gamma_b}|\alpha_s|^4 - \gamma_a = 0, \qquad \text{or} \qquad \boxed{|\alpha_s|^4 - \frac{3|\epsilon_b|}{\kappa}|\alpha_s| + \frac{3\gamma_a\gamma_b}{\kappa^2} = 0,} \tag{2.9}$$

which is a quartic I was able to solve on Wolfram Alpha.

Both the trivial and non-trivial solutions for $|\alpha_s|$ are plotted as a function of ϵ_b in Figure 2.4(a). We see that there are two non-trivial solutions, and that they are only realisable above some critical pumping threshold. There is no connection between the trivial and the non-trivial solutions. The two non-trivial solutions branch away from each other as the pumping increases, indicating that stronger pumping of the b mode can lead to either more or fewer photons in the a mode. However, we will see below that the lower branch is not stable. Note that the non-trivial solutions for α_s are triply degenerate due to the three different solutions for the phase. The results presented here are in agreement with those derived by *Bajer* [2].

Numerical Solution

In order to determine the steady states numerically, I used the `DifferentialEquations.jl` package for Julia to set up the coupled ODEs (2.2) as a `SteadyStateProblem`. This was solved for various values of ϵ_b, and the results are presented in Figure 2.4(b). Additionally, simulations of (2.2) were run, and the resulting steady states are also plotted in Figure 2.4(b). These numerical methods do not explicitly require $\gamma_b \gg \gamma_a$, but the same parameters are used as for the analytic result, so the condition still holds. The steady state solver is exactly consistent with the analytic solution,

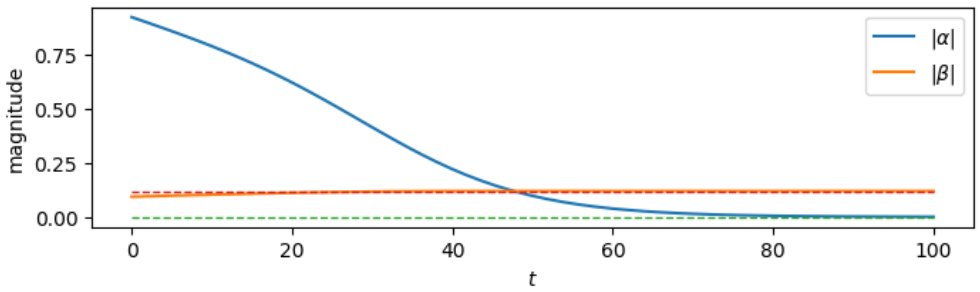

Figure 2.5: The time evolution of $|\alpha|$ and $|\beta|$ for an initial state taken to be on the "tail". Evidently this is not a steady state, as $|\alpha|$ and $|\beta|$ change over time. The dashed lines indicate the (stable) steady state values associated with the trivial $\alpha = 0$ solution.

except for an additional "tail" leading off from the bifurcation point. This is not a physical result, but rather a numeric issue, which can be seen by running a simulation of (2.2) with an initial state taken from the tail. The resulting time evolution is displayed in Figure 2.5, which shows that it is definitionally not a steady state.

The stability of the other solutions was tested numerically: the trivial solution and the upper branch are always stable, while the lower branch is unstable. These results are indicated in Figure 2.4(b), and match the analytic results presented in [2]. We see in Figure 2.4(b) that the simulations of (2.2) are consistent with the other results, and unsurprisingly lead to steady states corresponding only to the stable solutions. However, note that above the bifurcation point the trivial solution is stable, but there are no corresponding steady states from the simulation. To explain this it is useful to explicitly note that above the bifurcation point there are *two* stable solutions predicted by the steady state solver, but a simulation of the system can only ever finish in a *single* steady state. Variables such as the initial state of the system would affect which stable state is reached. For the simulation presented here, the initial state was $\alpha_0 = 1.2$, away from the vacuum so that we could take $\epsilon_a = 0$. A comparison of the steady states for various initial states is presented in Appendix D.1. As an extreme example, note that a simulation of a system with the initial state in the vacuum, and with $\epsilon_a = 0$, would have lead to steady states only on the $\alpha = 0$ solution.

The corresponding steady states for $|\beta|$ are given in Appendix D.2. They provide limited additional insight, but it is interesting to note that increasing ϵ_b leads to fewer b photons on the stable branch.

2.3.2 Original Parameters

We now return to the parameters $\kappa = 0.001$, and $\gamma_b = 2\gamma_a$. Their steady states were determined as a function of ϵ_b by running simulations of both the semi-classical ODEs (2.2), and the full truncated positive-P SDEs (1.59). The results are compared to those of the steady state solver introduced in Section 2.3.1. The analytic result from the previous section can not be used here because the $\gamma_b \gg \gamma_a$ condition does not hold. I begin by taking $\epsilon_a = 0$, as above, but finish by considering the effect of $\epsilon_a \neq 0$ on the steady states.

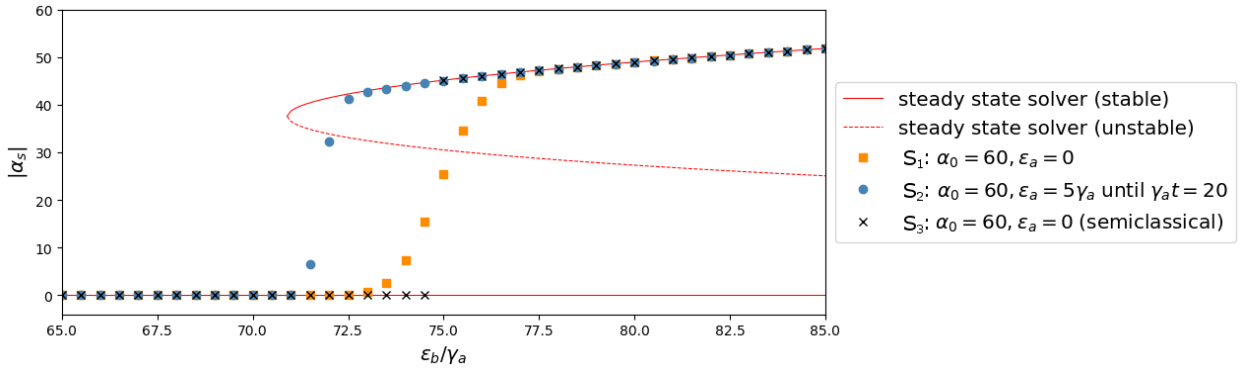

Figure 2.6: The steady states of $|\alpha|$ as a function of the pump intensity ϵ_b, as given by three simulations, and the steady state solver. The results only differ around the transition from the $\alpha = 0$ solution to the upper branch. Temporary introduction of $\epsilon_a \neq 0$ (blue circles) shifts the transition to lower ϵ_b. The corresponding steady state values for $|\beta|$ are presented in Appendix D.2. The parameters used are $\kappa = 0.001$ and$\gamma_b = 2\gamma_a$. The two stochastic simulations (blue circles and orange squares) were run until $\gamma_a t = 150$, and averaged over 20,000 trajectories.

Unpumped a mode

The steady states given by all three simulations, and the steady state solver, are presented in Figure 2.6 for the case that $\epsilon_a = 0$. The "tail" given by the steady state solver has been identified and removed. All three simulations had the initial state $\alpha = \alpha^+ = 60$, but differed in various ways:

- S_1: A stochastic simulation of the coupled SDEs (1.59), taking $\epsilon_a = 0$ always.
- S_2: A stochastic simulation of the coupled SDEs (1.59), taking $\epsilon_a = 5$ until $\gamma_a t = 20$. This may seem unnecessary, but the results are different from those of S_1, which leads to an interesting discussion.
- S_3: A simulation of the semi-classical coupled ODEs (2.2), with $\epsilon_a = 0$.

The general shape of the results given by the steady state solver is the same as those for the parameters used in Section 2.3.1. Away from the bifurcation point the simulations match the stable solutions extremely well, and as above, no simulation leads to a steady state on the unstable branch. This has been confirmed for ϵ_b ranging from 0 to $300\gamma_a$, but the range of values plotted is restricted in order to focus on the transition from the $\alpha = 0$ solution to the upper branch as ϵ_b is increased. In this region the simulations differ from each other and the steady state solver in two crucial ways. Firstly, the three simulations transition from the $\alpha = 0$ solution to the upper branch at different values of ϵ_b. Secondly, the stochastic simulations result in steady states at a seemingly continuous range of values between the two stable solutions predicted by the steady state solver. I refer to these steady states as the *intermediate values*. In order to understand these differences, it is important to remember that the stochastic simulations are averaged over 20,000 trajectories, so the steady states don't necessarily correspond to individual trajectories. This is emphasised in Figure 2.7, which shows the time evolution of S_1 for $\epsilon_b = 75\gamma_a$. We see that all the individual trajectories end at either $\alpha = 0$, or fluctuating around the upper branch. Whereas for most values of ϵ_b all the individual trajectories follow the same general path (neglecting small fluctuations), the intermediate values are a physically meaningful artefact of averaging over some trajectories that go up and some that go down.

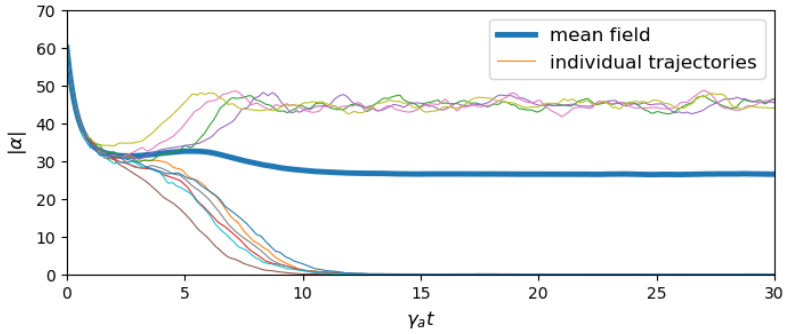

Figure 2.7: The time evolution of $|\alpha|$ for individual trajectories of the truncated positive-P SDEs (1.59), with comparison to the stochastic average over 20,000 trajectories. The individual trajectories always end up around the stable solutions predicted by the steady state solver, but their stochastic average has a steady state that does not correspond to a solution of the steady state solver. The parameters used are $\kappa = 0.001, \gamma_b = 2\gamma_a, \epsilon_a = 0$, and $\epsilon_b = 75\gamma_a$.

Notice that the value of ϵ_b at which the semi-classical steady states jump to the upper branch corresponds to the point at which half of the trajectories from S_1 are reaching the upper branch. This is because the two simulations correspond to an identical system[3]. However, S_2 corresponds to a system that has $\epsilon_a \neq 0$ until $\gamma_a t = 20$. To understand why it transitions to the upper branch at a smaller value of ϵ_b, it is useful to consider the time evolution of the three simulations, which is presented for selected values of ϵ_b in Figure 2.8. In S_1 the steady states are constant in time (i.e. they *are* steady states), indicating that, as expected, both the trivial solution and the upper branch are stable. In S_2, the inclusion of $\epsilon_a \neq 0$ has pushed some paths to the upper branch even though they go to $\alpha = 0$ in S_1 and S_3. When the pumping is turned off, most of the steady states remain in the upper branch because it is stable. However, close to the bifurcation point the upper branch is not actually stable for the SDEs (1.59), which can be seen by the fact that the $\epsilon_b = 71.5\gamma_a$ solution (orange line, Figure 2.8) tends towards the $\alpha = 0$ solution. In fact, the intermediate values for S_2 in Figure 2.6 are not in fact steady states - they correspond to paths that haven't reached $\alpha = 0$ yet[4]. All the paths corresponding to intermediate values in S_1 have had all trajectories pushed to the upper branch in S_2, where they are stable. In some respects there is no such thing as a stable solution for an SDE, but in practice we see that away from the bifurcation point the upper branch is essentially stable. From now on I will refer to this as "well above the critical pumping", even though we have shown there is no well defined critical pumping.

Finally, before considering the effect of including $\epsilon_a \neq 0$ in the steady state, I will briefly mention the transient behaviour of the time evolution itself. The simulations in Section 2.1 exhibited oscillatory behaviour before reaching their steady state, and this behaviour is also exhibited in Figure 2.8, but only for the larger values of ϵ_b. There is some kind of transition between an under-damped and over-damped regime, which coincides with the transition to the upper branch.

[3] As in Section 2.3.1, the initial state will affect the point at which this transition occurs. See Appendix D.1.

[4] Individual trajectories drop from the upper branch to the trivial solution rather fast, but the stochastic average moves rather slowly because it won't reach zero until all 20,000 trajectories have tunnelled away from the upper branch.

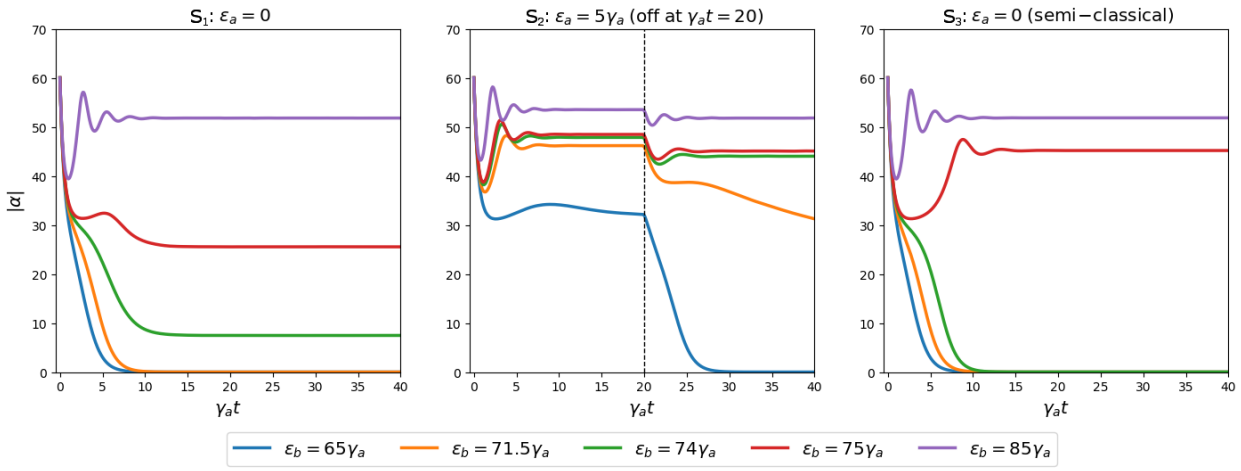

Figure 2.8: The time evolution of $|\alpha|$ for simulations $S_1 - S_3$ of the truncated positive-P SDEs (1.59) corresponding to five representative values of the pump intensity ϵ_b. The corresponding plots for $|\beta|$ are presented in Appendix D.3. The parameters used are $\kappa = 0.001$, and $\gamma_b = 2\gamma_a$, and 20,000 trajectories were averaged over for the stochastic simulations S_1 and S_2.

Pumped a mode

We now briefly look at the case in which the a mode is pumped in the steady state - primarily as an exploration of how the results differ from the unpumped case. Figure 2.9 shows the steady states as a function of ϵ_b as given by the steady state solver, for ϵ_a between $7\gamma_a$ and $12\gamma_a$. Both stable and unstable solutions are included, but the tail has been removed. The results are compared to those obtained via stochastic integration of the truncated positive-P SDEs (1.59).

For the lowest value, $\epsilon_a = 7\gamma_a$, the overall shape of the relationship is very similar to the unpumped case - the only differences are that the $\alpha = 0$ solution is now bounded below by approximately 7[5], and connects to the lower branch (around $\epsilon_b = 73\gamma_a$). As the pumping of the a mode increases, the connection to the $\alpha = 0$ solution moves closer to the bifurcation point, and above threshold ϵ_a, the upper branch and the $\alpha = 0$ solution merge into a single stable solution, and split away from the unstable solution. Interestingly, the shape of the unstable solution barely changes as ϵ_a is further increased.

Above the critical value of ϵ_a, where there is only one stable solution, the simulations are in agreement with the steady state solver. For smaller values of ϵ_a we observe the same pattern of intermediate values as the unpumped case.

2.4 Summary

In this chapter we considered the time evolution of the mode populations, and identified that they reached steady states. An analytical examination of the steady states in the over-damped regime produced results in agreement with the work of *Bajer* [2]. A careful numerical investigation of the steady states for a range of pump values near the critical pumping was performed using

[5] I will still refer to this solution as the $\alpha = 0$ solution however, as it is a useful label for distinguishing between the solutions.

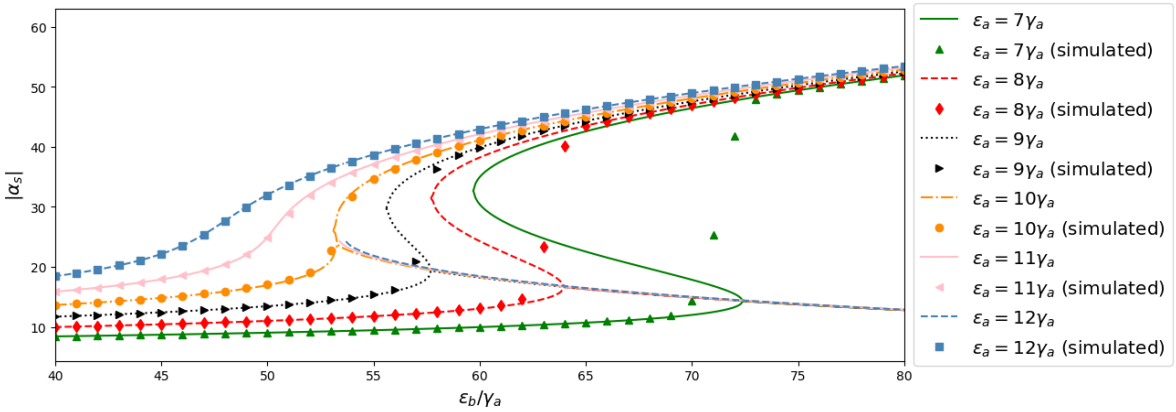

Figure 2.9: A comparison between the steady states as a function of the pump intensity ϵ_b predicted by both the steady state solver and stochastic integration of the truncated positive-P SDEs(1.59), for a range of ϵ_a. Above some critical value of ϵ_a there is only one stable solution, and two techniques are in close agreement. Below $\epsilon_a \approx 10$ the mean field permits intermediate values between the stable solutions. The parameters used are $\kappa = 0.001$, and $\gamma_b = 2\gamma_a$. The simulations were averaged over 20,000 trajectories, and run until $\gamma_a t = 150$.

both semi-classical and truncated positive-P phase space methods. We identified stable regions for the intra-cavity fields and showed that around the critical pumping quantum fluctuations shift the steady state populations away from semi-classical predictions. The importance of quantum fluctuations near critical values is well known in many other quantum optical systems. These results will be used in the following chapter to examine the squeezing and entanglement of the output fields as a function of ϵ_b.

Chapter 3

Steady State Fluctuation Analysis

As discussed in Chapter 2, the expected number of photons in each mode has a well defined steady state. In this section we consider fluctuations of the output field about the steady state mean field. In particular this provides insight into the squeezing and entanglement of the modes, both of which are experimentally measurable quantities of interest. We exploit the fact that the the steady state is described by a stationary process, and consider the spectrum of fluctuations by looking at the covariance matrix (defined in Section 1.4.1) as a function of frequency rather than time. I begin by considering the fixed set of parameters used in Section 2.1: $\kappa = 0.001, \gamma_b = 2\gamma_a, \epsilon_a = 0$, and $\epsilon_b = 200\gamma_a$, then investigate the squeezing and entanglement as a function of ϵ_b in Section 3.3.

In order to consider fluctuations about the steady state, we explicitly write the phase space variables in terms of their steady state expectation values plus some small fluctuation:

$$\boldsymbol{\alpha}(t) = \langle \boldsymbol{\alpha} \rangle_s + \delta\boldsymbol{\alpha}(t), \tag{3.1}$$

where $\boldsymbol{\alpha} \equiv (\alpha, \alpha^+, \beta, \beta^+)$, $\langle \boldsymbol{\alpha} \rangle_s$ is a corresponding vector of steady state values, and $\delta\boldsymbol{\alpha}$ is a corresponding vector of small time-dependent fluctuations. Note that due to the time-independent nature of $\langle \boldsymbol{\alpha} \rangle_s$, the time evolution of $\delta\boldsymbol{\alpha}$ will be the same as that of $\boldsymbol{\alpha}$ up to a constant offset. We assume that the fluctuations are relatively small, allowing us to linearise the equation of motion. In order to determine the time evolution of the fluctuations, we begin with the coupled SDEs (1.59), and linearise the time evolution of $\boldsymbol{\alpha}$ due to the drift and diffusion terms separately:

Drift: When considering the time evolution due to the the drift terms in (1.59), we drop any terms of second order or higher with respect to the fluctuation terms[1]:

$$\begin{aligned}
\dot{\alpha}_{\text{drift}} &= -\gamma_a\alpha + \kappa\alpha^{+2}\beta, \\
&= -\gamma_a(\alpha_s + \delta\alpha) + \kappa(\alpha_s^* + \delta\alpha^+)(\alpha_s^* + \delta\alpha^+)(\beta_s + \delta\beta), \\
&= -\gamma_a\alpha_s - \gamma_a\delta\alpha + \kappa[\alpha_s^{*2}\beta_s + 2\alpha_s^*\beta_s\delta\alpha^+ + \delta\alpha^{+2}\beta_s + \alpha_s^{*2}\delta\beta + 2\alpha_s^*\delta\alpha^+\delta\beta + \delta\alpha^{+2}\delta\beta], \\
&\approx -\gamma_a\alpha_s - \gamma_a\delta\alpha + \kappa[\alpha_s^{*2}\beta_s + 2\alpha_s^*\beta_s\delta\alpha^+ + \alpha_s^{*2}\delta\beta], \\
&= \dot{\alpha}_s - \gamma_a\delta\alpha + 2\kappa\alpha_s^*\beta_s\delta\alpha^+ + \kappa\alpha_s^{*2}\delta\beta, \qquad \text{where } \dot{\alpha}_s \equiv 0 \text{ by definition}, \\
&= -\gamma_a\delta\alpha + 2\kappa\alpha_s^*\beta_s\delta\alpha^+ + \kappa\alpha_s^{*2}\delta\beta.
\end{aligned}$$

[1] Note that we take $\alpha_s^+ = \alpha_s^*$ in the semi-classical limit of many photons.

The other terms are derived analogously, and given by

$$\begin{aligned}\dot{\alpha}^{+}_{\text{drift}} &= -\gamma_a \delta\alpha^{+} + 2\kappa\alpha_s\beta_s^{*}\delta\alpha + \kappa\alpha_s^{*2}\delta\beta,\\ \dot{\beta}_{\text{drift}} &= -\gamma_b \delta\beta - \kappa\alpha_s^{2}\delta\alpha,\\ \dot{\beta}^{+}_{\text{drift}} &= -\gamma_b \delta\beta - \kappa\alpha_s^{*2}\delta\alpha^{+}.\end{aligned}$$

Diffusion: When considering the time evolution due to the diffusion terms in (1.59), we have

$$\dot{\alpha}_{\text{diff}} = \sqrt{2\kappa\alpha^{+}\beta}\,\xi_1 = \sqrt{2\kappa(\alpha_s^{+} + \delta\alpha^{+})(\beta_s + \delta\beta)}\,\xi_1, \tag{3.2}$$

and analogously for $\dot{\alpha}^{+}$. The β and β^{+} equations have no diffusion terms. Far above critical pumping, the fluctuation terms will be much smaller than the steady state values, so we approximate this term by neglecting them. So the two diffusion terms are

$$\dot{\alpha}_{\text{diff}} = \sqrt{2\kappa\alpha_s^{*}\beta_s}\,\xi_1, \tag{3.3}$$

$$\dot{\alpha}^{+}_{\text{diff}} = \sqrt{2\kappa\alpha_s\beta_s^{*}}\,\xi_1. \tag{3.4}$$

It is important to note that this argument would not have held for the drift terms because, after linearisation, the remaining steady state terms summed to zero, leaving only the fluctuation terms. It may also seem that this argument does not apply to the a mode below the critical pumping. However, for the reason that $\alpha = 0$ here, i.e. the a mode is in the vacuum, there are no fluctuations (the only uncertainty, as we will see, is the inherent uncertainty of the vacuum).

Putting these all together, we see that we can write

$$\frac{d\,\delta\boldsymbol{\alpha}}{dt} = -A\,\delta\boldsymbol{\alpha} + B\,\boldsymbol{\xi}(t) \qquad \longleftrightarrow \qquad d\,\delta\boldsymbol{\alpha} = -A\,\delta\boldsymbol{\alpha}\,dt + B\,d\mathbf{W}, \tag{3.5}$$

where

$$A = \begin{bmatrix} \gamma_a & -2\kappa\alpha_s^{*}\beta_s & -\kappa\alpha_s^{*2} & 0 \\ -2\kappa\alpha_s\beta_s^{*} & \gamma_a & 0 & -\kappa\alpha_s^{2} \\ \kappa\alpha_s^{2} & 0 & \gamma_b & 0 \\ 0 & \kappa\alpha_s^{*2} & 0 & \gamma_b \end{bmatrix}, \qquad BB^{T} = D = \begin{bmatrix} 2\kappa\alpha_s^{*}\beta_s & 0 & 0 & 0 \\ 0 & 2\kappa\alpha_s\beta_s^{*} & 0 & 0 \\ 0 & 0 & 0 & 0 \\ 0 & 0 & 0 & 0 \end{bmatrix}. \tag{3.6}$$

Note that in the linearised equation of motion, (3.5), the drift vector has the form of a constant matrix, A, multiplied by $\delta\boldsymbol{\alpha}$, and that the drift matrix, B, is a constant with no dependence on $\delta\boldsymbol{\alpha}$. This is the form of a multivariate *Ornstein-Uhlenbeck process*, which is a well known subset of stochastic differential equations. It is shown in [9, 11] that the covariance spectrum of a multivariate Ornstein-Uhlenbeck process is given by

$$S(\omega) = (A + i\omega\mathbb{1})^{-1} BB^{T} (A^{\dagger} - i\omega\mathbb{1})^{-1}, \tag{3.7}$$

with A and B defined in (3.6), and $\mathbb{1}$ the identity matrix. Currently, (3.7) is the spectrum with respect to the creation and annihilation operators, which are not Hermitian, so cannot correspond to

physical observables. It is therefore desirable to write the spectrum with respect to the quadrature operators defined in Section 1.3.5. This is given by [1, 10]

$$S^q(\omega) = QS(\omega)Q^T, \qquad \text{where} \quad Q = \begin{bmatrix} 1 & 1 & 0 & 0 \\ -i & i & 0 & 0 \\ 0 & 0 & 1 & 1 \\ 0 & 0 & -i & i \end{bmatrix}. \tag{3.8}$$

The elements of $S^q(\omega)$ tell us the covariances of the quadrature operators *within the cavity*, where the interaction is taking place. The *output* spectra, which is what would be measured experimentally, is related to the intra-cavity spectra via the damping rates of the modes [14, 10], so the covariances that would be experimentally measured are

$$\mathrm{C}[\hat{X}_i, \hat{X}_j](\omega) = \delta_{ij} + \sqrt{\gamma_i \gamma_j}(S^q_{i,j} + S^q_{j,i}), \tag{3.9}$$

and similarly for the $\hat{Y}$ quadratures. The second term in (3.9) gives the (output) covariances due to the interaction, which have been derived above, while the Kronecker delta corresponds to the variance due to the background uncertainty of the vacuum: from Section 1.3.5 we know $\Delta X_i = 1$ in the vacuum, so $C[\hat{X}_i, \hat{X}_i] = V[\hat{X}_i] = \Delta X_i^2 = 1$, while $C[\hat{X}_i, \hat{X}_j] = 0$ because the two modes are uncorrelated in the vacuum.

3.1 Squeezing

The first property of the output fields we examine is the *squeezing* of both modes. Recall from Section 1.3.5 that a mode is squeezed if measurements of either of its quadrature operators have a variance of less than one. Using the steady states from the simulations in Section 2.1 to construct the spectrum matrix, the variance of each quadrature is shown as a function of frequency in Figure 3.1. Both $\hat{Y}$ quadratures have variances less than one, which means that both modes are in a *squeezed state*. It has been verified that $\Delta X_a \Delta Y_a \geq 1$ and $\Delta X_b \Delta Y_b \geq 1$ for all frequencies, which can qualitatively be seen by the fact that the variance in the $\hat{X}$ quadratures increases significantly when the variance in the $\hat{Y}$ quadratures dips.

The results presented in Figure 3.1 correspond to steady states in which the low energy mode is pumped, albeit significantly less than the high energy mode. As a comparison, Figure 3.2 presents these results alongside the case that $\epsilon_a = 0$. Removing the pumping leads to slightly increased squeezing, but the overall spectrum is unaffected. It has been verified that the uncertainty products are greater than one for all frequencies in the unpumped case.

3.2 Bipartite Entanglement

The other property of the output fields we consider is whether the high and low energy modes are *entangled*. In order to investigate this, we use the Duan-Simon inequality [15, 16]:

$$\mathrm{DS}_\pm \equiv \mathrm{V}(\hat{X}_i \pm \hat{X}_j) + \mathrm{V}(\hat{Y}_i \mp \hat{Y}_j) \geq 4, \tag{3.10}$$

which holds for classically behaved states. It is known that if either DS_+ or DS_- are *violated*, then the two fields are entangled. Figure 3.3 shows $\mathrm{DS}_\pm$ as a function of frequency for both $\epsilon_a = 0$ and 5. We see that in both cases the DS_- inequality is violated in two frequency regimes, indicating that the fields are entangled.

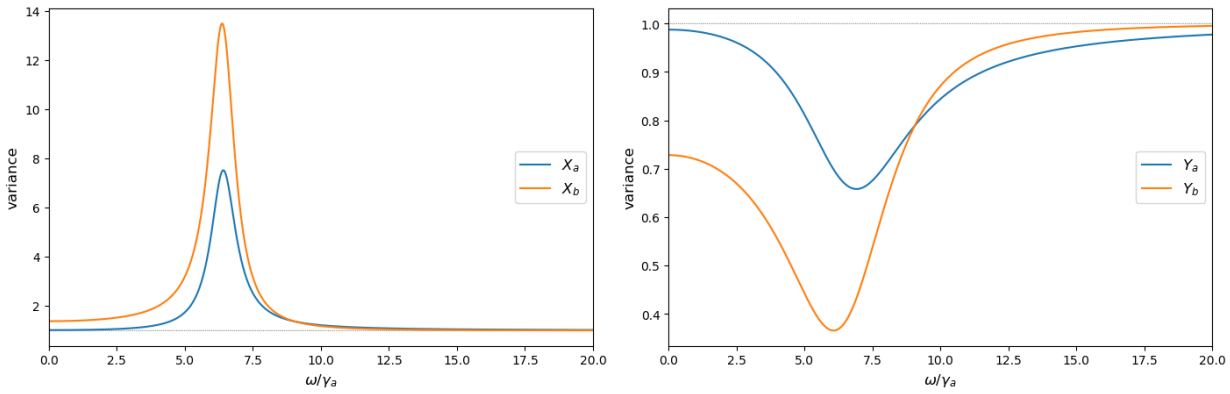

(a) $\hat{X}$ quadratures (b) $\hat{Y}$ quadratures

Figure 3.1: The spectrum of quadrature variances, calculated using (3.9) for steady states obtained by simulations of the semi-classical approximation (2.2). Both $\hat{Y}$ quadratures have variances less than one, which is to say that both modes are squeezed. The parameters used are $\kappa = 0.001, \gamma_b = 2\gamma_a, \epsilon_a = 5\gamma_a$, and $\epsilon_b = 200\gamma_a$.

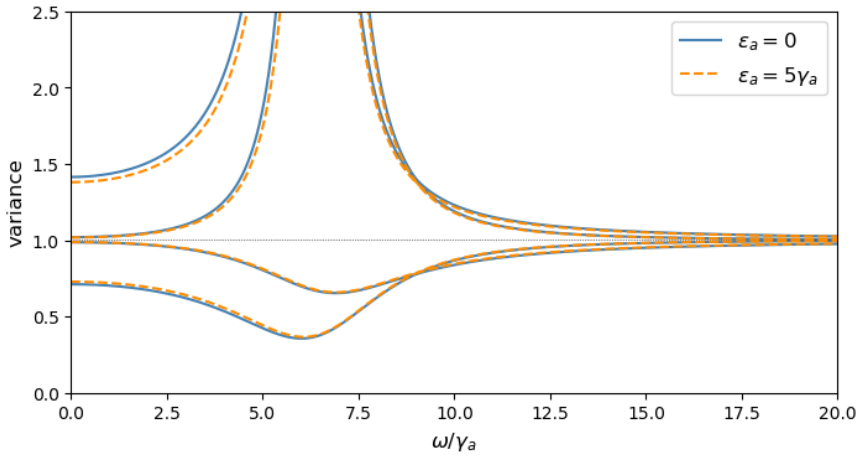

Figure 3.2: A comparison between the quadrature variances when the low energy mode is and is not pumped ($\epsilon_a = 5\gamma_a$ and 0 respectively). The $\epsilon_a = 5\gamma_a$ results are a replication of those presented in Figure 3.1. The overall form of the spectrum is unaffected. The parameters used are $\kappa = 0.001, \gamma_b = 2\gamma_a, \epsilon_a = 5\gamma_a$, and $\epsilon_b = 200\gamma_a$.

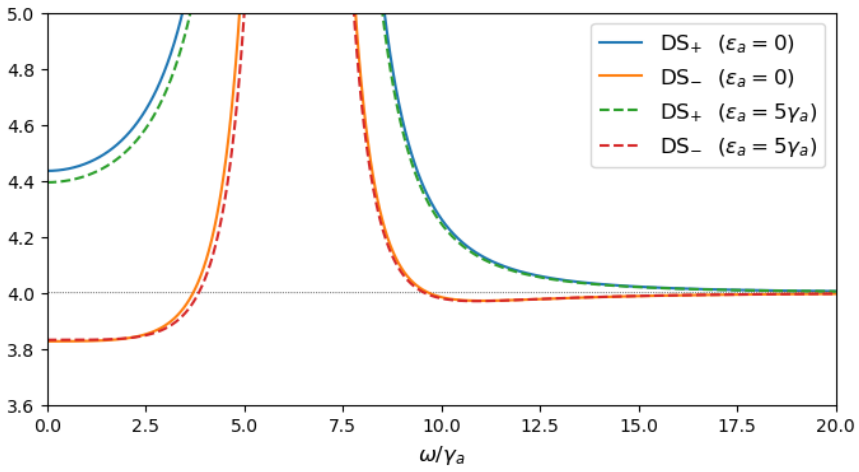

Figure 3.3: The Duan-Simon spectra for the cases when the low energy mode is and isn't pumped ($\epsilon_a = 5\gamma_a$ and 0 respectively), calculated using (3.10) for steady states obtained by simulations of the semi-classical approximation (2.2). The DS$_-$ inequality is violated in two frequency regimes, indicating entanglement between the modes. The inclusion of $\epsilon_a = 5\gamma_a$ has a minimal effect. The parameters used are $\kappa = 0.001, \gamma_b = 2\gamma_a$, and $\epsilon_b = 200\gamma_a$.

3.3 Effect of Pumping Strength

In this section, I present a systematic analysis of the squeezing and entanglement of the modes in degenerate triplet down conversion as a function of the pump intensity of the high energy mode. As shown in Section 2.3.2, the steady states of the system depend on various quantities such as the initial state of the system, and any pumping of the a mode. The following discussion focuses on systems with $\epsilon_a = 0$ in the steady state.

The overall behaviour of the spectra is investigated using the steady states obtained by the semi-classical simulation S_3 from Section 2.3.2. The semi-classical simulation provides a set of physical steady states, but neglects some of the interesting behaviour that can occur around the critical pumping, so a careful study of the critical region is also presented using the truncated positive-P approach. This is achieved using the steady states given by simulation S_1, which correspond to the orange squares in Figure 2.6, and with time evolution given in Figure 2.8(a).

3.3.1 Semi-Classical Simulations

Squeezing: Figure 3.4 shows the spectrum of variances of the X and Y quadratures for both modes as a function of ϵ_b. Both X quadratures display the same behaviour, as do both Y quadratures, although the magnitude is consistently larger for the b quadrature. We see that below the critical pumping all four quadratures have a variance 1, i.e. that of the vacuum. This is unsurprising because the a mode is in a vacuum state below the critical pumping, which corresponds to a minimum uncertainty state. At the same time, the b mode will be a pure coherent state (as it is being coherently pumped with no down conversion), which is also a minimum uncertainty state. Above the critical pumping both Y quadratures have a variance less than one at all values of ϵ_b, indicating that both modes are always squeezed. The magnitude of the squeezing reduces as the pumping increases, and the maximal squeezing moves towards larger frequencies. Immediately

above the critical pumping the b mode is maximally squeezed at zero frequency, while the peak squeezing of the a mode is away from zero frequency.

Entanglement: The bipartite entanglement between the modes is investigated using the Duan-Simon inequalities (3.10). The results are presented in Figure 3.6, where we observe similar behaviour to the squeezing. The DS_- inequality is never violated, but the DS_+ inequality is violated, implying the two modes are entangled, for all values of ϵ_b above the critical pumping.

3.3.2 Stochastic Simulations

I now consider the results of the stochastic positive-P simulation S_1 (with steady states corresponding to the orange squares in Figure 2.6, and with time evolution given in Figure 2.8(a)). In Section 2.3.2 we saw that away from the transition region, these steady states matched those of the semi-classical simulation exactly. Therefore, the results presented in this section will focus on the region $65\gamma_a \leq \epsilon_b \leq 85\gamma_a$, about the critical pumping, where the results differ significantly from Section 3.3.1 due to the stronger effects of quantum fluctuations near critical pumping.

Squeezing: The variance of each of the four quadratures is presented as a function of ϵ_b in Figure 3.5. In all four plots we see that, as would be expected, there is no well defined critical pumping, and that the dominant behaviour is actually located within the transition region. Considering the X quadratures, we see that both modes have their greatest variance in the transition region, and that this occurs about zero frequency (i.e. the long time limit). Turning to the Y quadratures we see that both modes are squeezed in the transition region, but the behaviour is different for each mode. Whereas the squeezing of the b mode gradually decreases with ϵ_b in the transition region, the a mode exhibits its strongest squeezing in the transition region. Additionally, this occurs around zero frequency, corresponding to the long time limit.

Entanglement: $\mathrm{DS}_\pm$ are presented as a function of ϵ_b in Figure 3.7. Both spike abruptly around zero frequency in the transition region about zero frequency. Entanglement extends partially into the transition region, but is otherwise relatively unaffected.

3.4 Summary

In this chapter we calculated the spectrum of covariances from the steady states of various simulations in Chapter 2. This was used to determine the squeezing of both the high and low energy modes, and their entanglement to each other in the output field. Semi-classical steady states provided results well above the critical pumping, while truncated positive-P steady states were used to correct for quantum fluctuations in the transition region. Below critical pumping, both modes are in a minimum uncertainty state. We found the fields to be squeezed and entangled at all values of ϵ_b corresponding to states with non-zero populations of a mode photons.

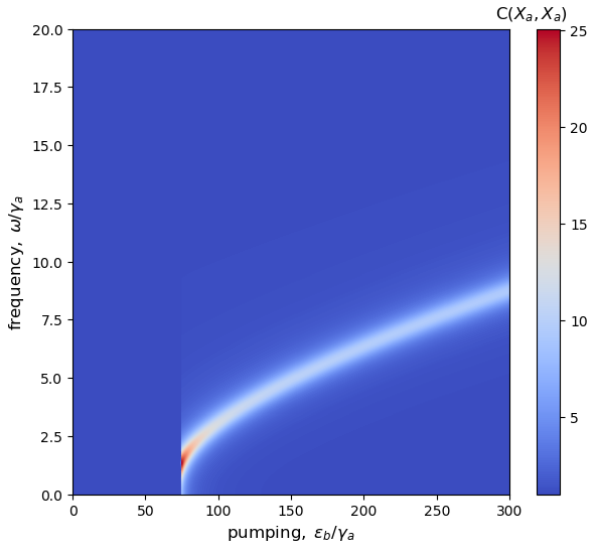

(a) X_a quadrature variance

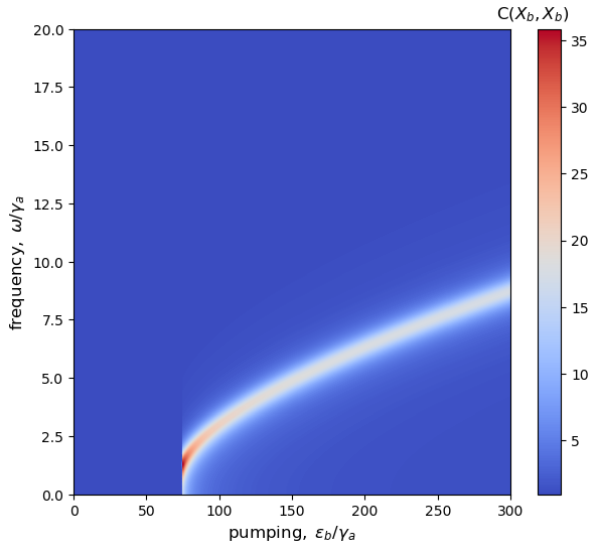

(b) X_b quadrature variance

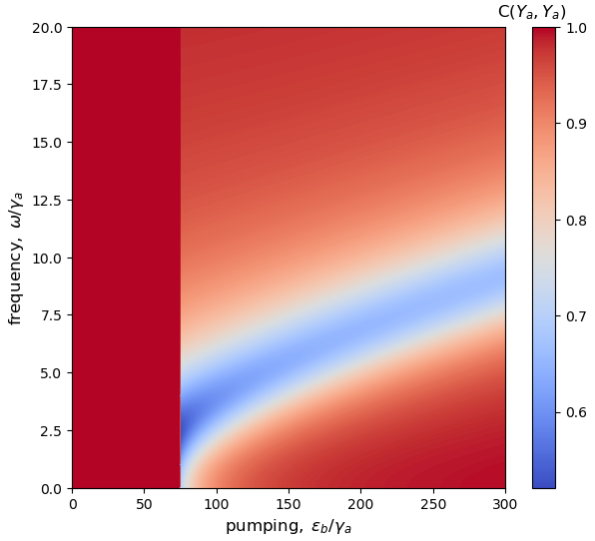

(c) Y_a quadrature variance

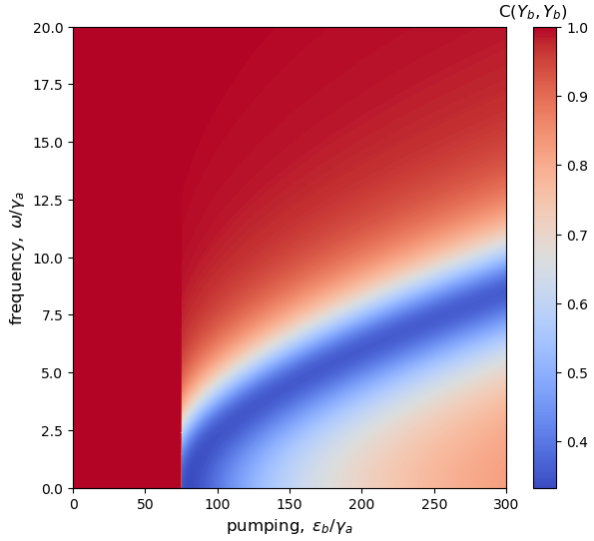

(d) Y_b quadrature variance

Figure 3.4: The spectrum of quadrature variances as a function of the pump intensity ϵ_b, calculated using (3.9) for steady states obtained from the semi-classical simulation S_3. Note the scale differs between plots. The system is most squeezed close to the critical pumping. Figure 3.5 examines the region around the critical pumping using the stochastic simulation S_1. The parameters used are $\kappa = 0.001, \gamma_b = 2\gamma_a$, and $\epsilon_a = 0$.

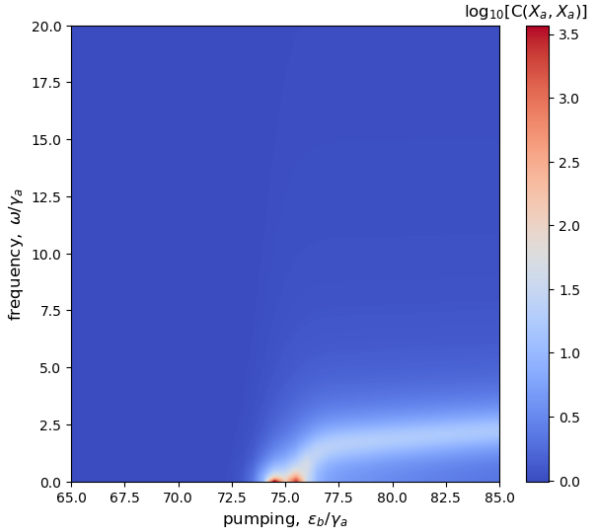

(a) X_a quadrature variance

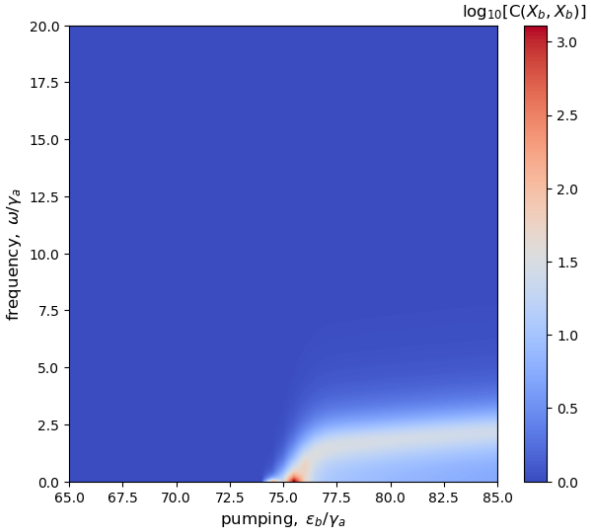

(b) X_b quadrature variance

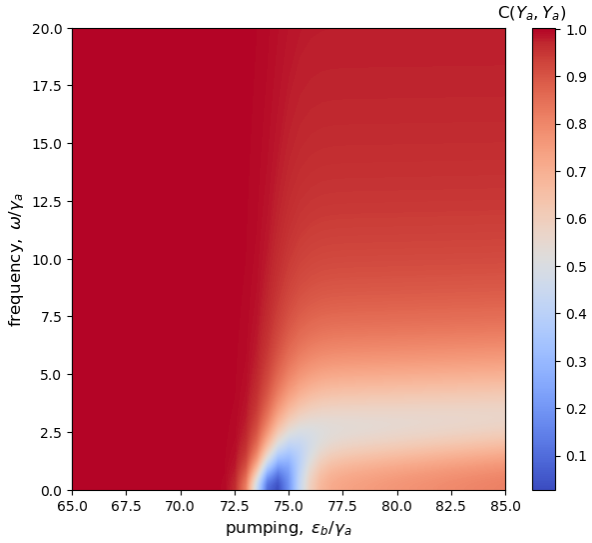

(c) Y_a quadrature variance

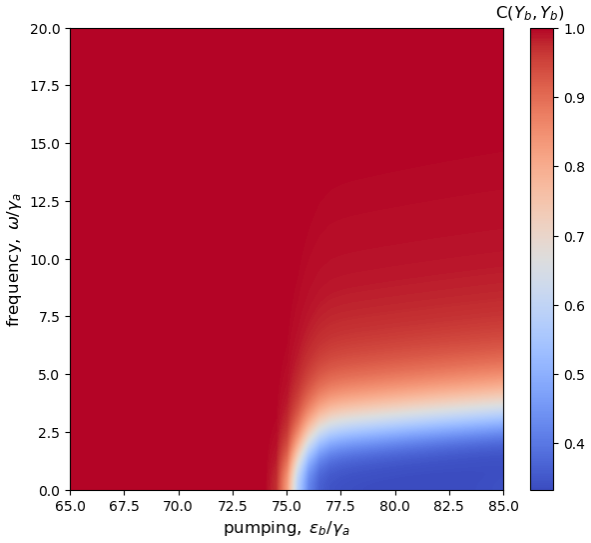

(d) Y_b quadrature variance

Figure 3.5: The spectrum of quadrature variances as a function of the pump intensity ϵ_b, calculated using (3.9) for steady states obtained from the stochastic simulation S_3. A log scale is used for the X quadratures for ease of visualisation. The a mode is strongly squeezed in the transition region, but squeezing of the b mode is essentially unaffected. The parameters used are $\kappa = 0.001, \gamma_b = 2\gamma_a$, and $\epsilon_a = 0$. 20,000 trajectories were averaged over.

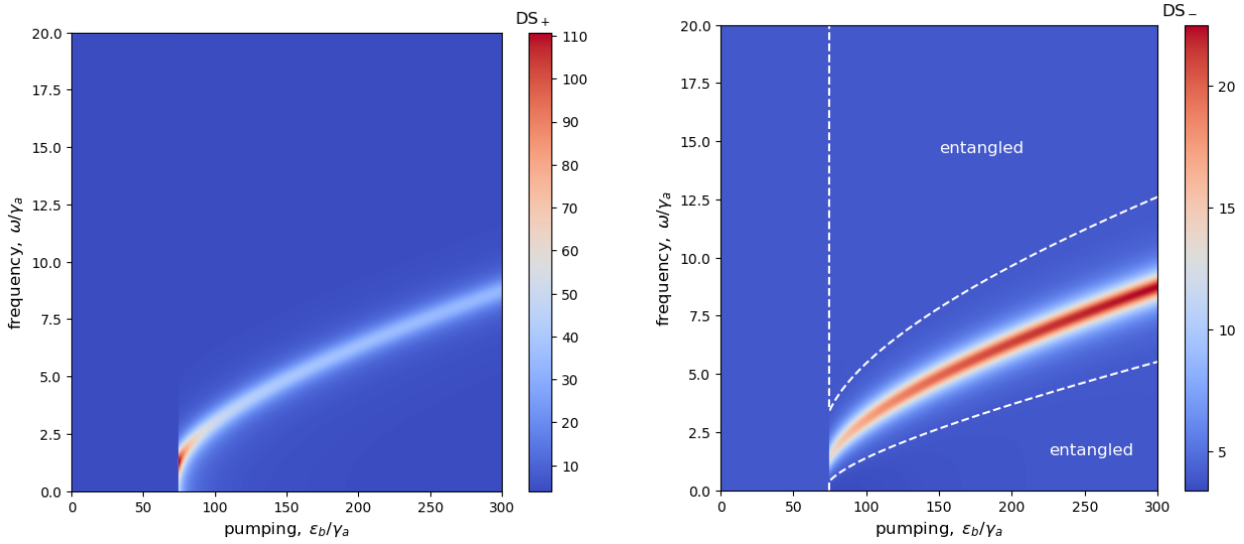

Figure 3.6: The Duan-Simon spectra as a function of the pump intensity ϵ_b, calculated using (3.10) for steady states obtained from the semi-classical simulation S_3. The two modes are entangled at all values of ϵ_b above the critical pumping. Figure 3.7 examines the region around the critical pumping using the stochastic simulation S_1. The parameters used are $\kappa = 0.001, \gamma_b = 2\gamma_a$, and $\epsilon_a = 0$.

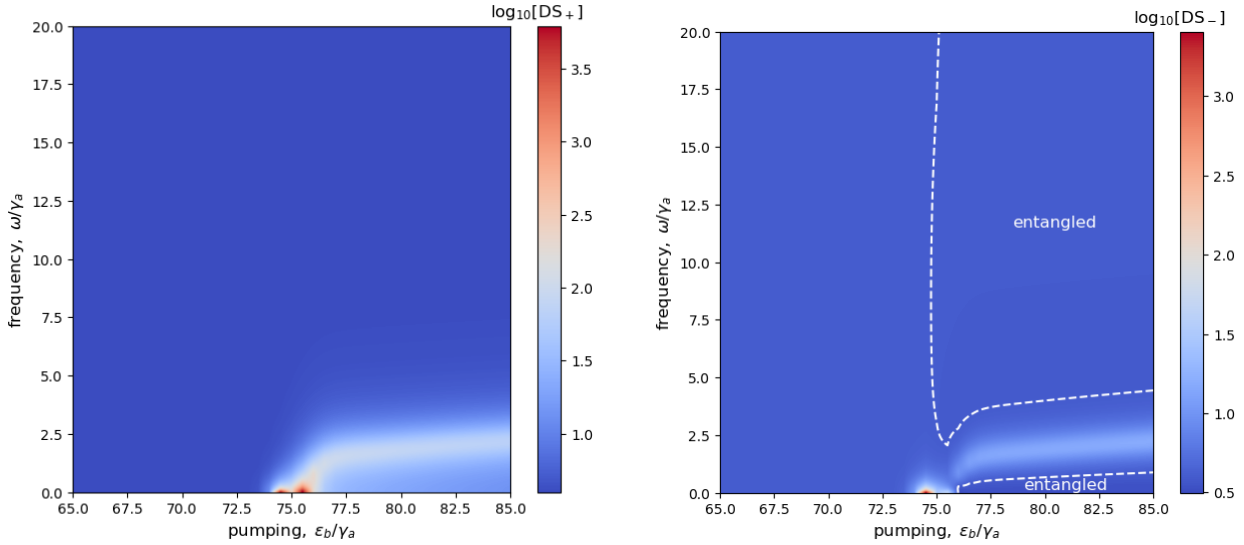

(a) DS_+ (b) DS_-

Figure 3.7: The Duan-Simon spectra as a function of the pump intensity ϵ_b, calculated using (3.10) for steady states obtained from the stochastic simulation S_1.A log scale is used for ease of visualisation. The modes are entangled part way into the transition region. The parameters used are $\kappa = 0.001, \gamma_b = 2\gamma_a$, and $\epsilon_a = 0$. 20,000 trajectories were averaged over.

Chapter 4

Non-Degenerate Triplet Down Conversion

Chapters 2 and 3 have considered the process of degenerate triplet down conversion, in which the three down-converted photons are indistinguishable and the time evolution is governed by (1.59) in the truncated positive P representation. This chapter turns to examine the process of *non-degenerate* triplet down conversion, in which the three down-converted photons are distinguishable, namely in energy (frequency). The interaction Hamiltonian is the natural generalisation of the degenerate case

$$\hat{H}_{\text{int}} = i\hbar\kappa \left[\hat{a}_1^\dagger \hat{a}_2^\dagger \hat{a}_2^\dagger \hat{b} - \hat{b}^\dagger \hat{a}_1 \hat{a}_2 \hat{a}_3\right], \tag{4.1}$$

and pumping of all four modes is modelled via the inclusion of four pumping Hamiltonians, analogous to (1.55). When mapped into optical phase space using the positive-P representation, the resulting PDE has third order derivatives [1], but we perform the usual truncation procedure and arrive at the following SDE[1] [1]

$$\begin{aligned}
\dot{\alpha}_1 &= \epsilon_1 - \gamma_1\alpha_1 + \kappa\alpha_2^+\alpha_3^+\beta + \sqrt{\kappa\alpha_3^+\beta/2}(\xi_1 + i\xi_2) + \sqrt{\kappa\alpha_2^+\beta/2}(\xi_3 + i\xi_4),\\
\dot{\alpha}_1^+ &= \epsilon_1^* - \gamma_1\alpha_1^+ + \kappa\alpha_2\alpha_3\beta^+ + \sqrt{\kappa\alpha_3\beta^+/2}(\xi_5 + i\xi_6) + \sqrt{\kappa\alpha_2\beta^+/2}(\xi_7 + i\xi_8),\\
\dot{\alpha}_2 &= \epsilon_2 - \gamma_2\alpha_2 + \kappa\alpha_1^+\alpha_3^+\beta + \sqrt{\kappa\alpha_3^+\beta/2}(\xi_1 - i\xi_2) + \sqrt{\kappa\alpha_1^+\beta/2}(\xi_9 + i\xi_{10}),\\
\dot{\alpha}_2^+ &= \epsilon_2^* - \gamma_2\alpha_2^+ + \kappa\alpha_1\alpha_3\beta^+ + \sqrt{\kappa\alpha_3\beta^+/2}(\xi_5 - i\xi_6) + \sqrt{\kappa\alpha_1\beta^+/2}(\xi_{11} + i\xi_{12}),\\
\dot{\alpha}_3 &= \epsilon_3 - \gamma_3\alpha_3 + \kappa\alpha_1^+\alpha_2^+\beta + \sqrt{\kappa\alpha_2^+\beta/2}(\xi_3 - i\xi_4) + \sqrt{\kappa\alpha_1^+\beta/2}(\xi_9 - i\xi_{10}),\\
\dot{\alpha}_3^+ &= \epsilon_3^* - \gamma_3\alpha_3^+ + \kappa\alpha_1\alpha_2\beta^+ + \sqrt{\kappa\alpha_2\beta^+/2}(\xi_7 - i\xi_8) + \sqrt{\kappa\alpha_1\beta^+/2}(\xi_{11} - i\xi_{12}),\\
\dot{\beta} &= \epsilon_b - \gamma_b\beta - \kappa\alpha_1\alpha_2\alpha_3,\\
\dot{\beta} &= \epsilon_b^* - \gamma_b\beta^+ - \kappa\alpha_1^+\alpha_2^+\alpha_3^+.
\end{aligned} \tag{4.2}$$

Inspection of (4.2) shows that the process will not proceed from the vacuum unless at least two of the low energy modes are pumped[2], so my simulations include weak[3] pumping of both the a_1

[1] Note that this SDE has non-diagonal noise, which is in contrast to the degenerate case: each equation in (1.59) has its own noise term, while there is mixing of noise terms between equations in (4.2).

[2] As above, this is a result of truncation.

[3] As in Chapter 2, "weak" here refers to $\epsilon_1, \epsilon_2 \ll \epsilon_b$.

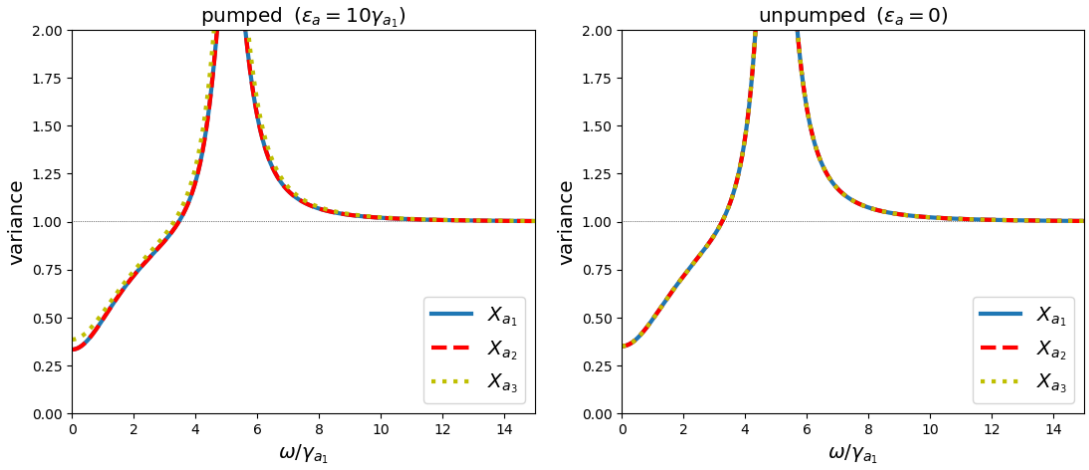

Figure 4.1: The spectrum of variances for the three X_a quadratures in the cases when the a_1 and a_2 modes are pumped and not pumped in the steady state ($\epsilon_{a_1}, \epsilon_{a_2} = 10\gamma_{a_i}$ and 0 respectively). The other parameters used are $\kappa = 0.001, \gamma_b = 2\gamma_{a_i}$, and $\epsilon_b = 200\gamma_{a_i}$.

and a_2 modes. This can be turned off once the system is in the steady state. I began by solving (4.2) using the SDE solvers in `DifferentialEquations.jl`, but it was unstable, so I could not run many trajectories. However, we know that for the degenerate case the semi-classical ODE gave steady state results consistent with the full stochastic SDE, and ultimately I am most interested in the steady state, so I have instead used the following semi-classical ODE

$$\begin{aligned}
\dot{\alpha}_1 &= \epsilon_1 - \gamma_1\alpha_1 + \kappa\alpha_2^*\alpha_3^*\beta, \\
\dot{\alpha}_2 &= \epsilon_2 - \gamma_2\alpha_2 + \kappa\alpha_1^*\alpha_3^*\beta, \\
\dot{\alpha}_3 &= \epsilon_3 - \gamma_3\alpha_3 + \kappa\alpha_1^*\alpha_2^*\beta, \\
\dot{\beta} &= \epsilon_b - \gamma_b\beta + \kappa\alpha_1\alpha_2\alpha_3,
\end{aligned} \tag{4.3}$$

which is obtained by dropping the stochastic terms and taking the initial condition to be a coherent state. The steady state spectra of squeezing and entanglement obtained from this semi-classical approach are presented below. Throughout this chapter we take $\gamma_{a_i} = 1$ for all three low energy modes, which provides a characteristic time scale for all parameters and simulations.

4.1 Squeezing

We begin by considering the squeezing of the low energy modes. Figure 4.1 shows the variance of the three X quadratures for systems both with and without pumping in the steady state. In the pumped case the X_{a_3} quadrature differs slightly from the other two because only the a_1 and a_2 modes are pumped. In the case that the pumping is removed, all three modes unsurprisingly have the same spectrum. Importantly, all three of the low energy modes are squeezed in both cases. For completeness, Figure 4.2 shows the variance of the three Y_a quadratures. We see that there is a region where the variance of the Y_a quadratures is less than one, contributing to the squeezing of the modes. It has been confirmed that the uncertainty principle is not violated at any frequency.

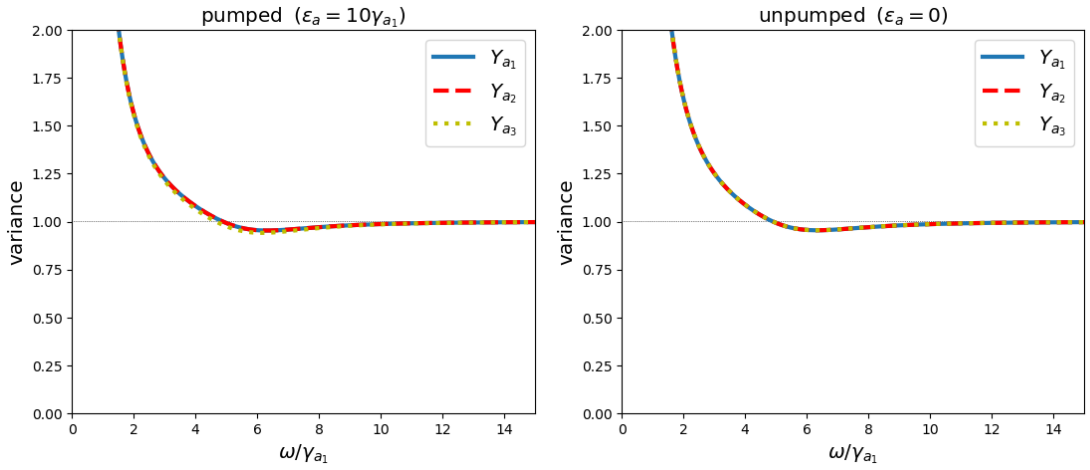

Figure 4.2: The spectrum of variances for the three Y_a quadratures in the cases when the a_1 and a_2 modes are pumped and not pumped in the steady state ($\epsilon_{a_1}, \epsilon_{a_2} = 10\gamma_{a_i}$ and 0 respectively). The other parameters used are $\kappa = 0.001, \gamma_b = 2\gamma_{a_i}$, and $\epsilon_b = 200\gamma_{a_i}$.

It is important to note the differences from the degenerate case. Firstly, in the degenerate case we only ever had $\Delta Y < 1$, but in this case both quadratures have regions where they have variances less than one. Secondly, in the degenerate case the squeezing is most pronounced for frequency elements around $\omega/\gamma_a = 5$, while here it is about zero frequency, which corresponds to the long time limit.

We now consider the squeezing of the b mode. Figure 4.3 shows the variance of both the X_b and Y_b quadratures in the case of both pumping and no pumping of the low energy modes. In both cases the Y_b quadrature has a variance of less than one, indicating that the b mode is squeezed. Comparing the pumped case to the results in Figure 3.1, we see that the spectrum of variances for the b mode is very similar to the degenerate case. However, there is a key difference in the pumped system - the Y_b quadrature has a spike in its variance at zero frequency. It appears as though the squeezing of the b mode is strongly dependent on the quantum state of the a mode in the steady state. The decrease in squeezing occurs around zero frequency, which is consistent with the inclusion of a constant pumping to the a mode (a feature at zero frequency).

4.2 Entanglement

We now turn to consider entanglement in the non-degenerate system. In the degenerate case, we investigated the bipartite entanglement between the modes using the Duan-Simon inequality (3.10). I did the same for every combination of two modes for the non-degenerate case, but found no evidence of any bipartite entanglement.

However, now that there are more than two distinct modes, we can also consider multipartite entanglement. When dealing with systems of more than two distinct modes, the discussion of entanglement is more complicated because there is the idea of partially-separable states. There are various measures that can be used to quantify the entanglement, but for the purposes of this

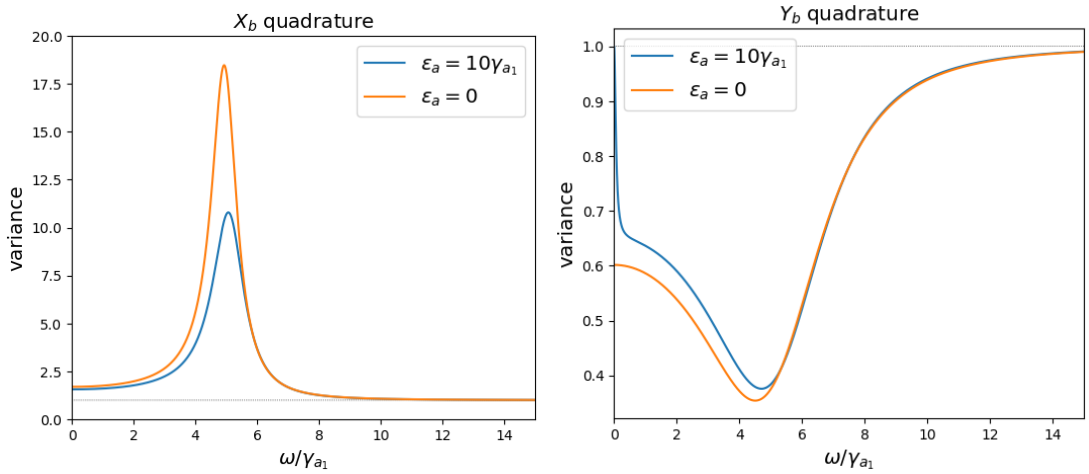

(a) X_b quadrature

(b) Y_b quadrature

Figure 4.3: The spectrum of quadrature variances for b mode in the cases when the a_1 and a_2 modes are pumped and not pumped in the steady state ($\epsilon_{a_1}, \epsilon_{a_2} = 10\gamma_{a_i}$ and 0 respectively). The other parameters used are $\kappa = 0.001, \gamma_b = 2\gamma_{a_i}$, and $\epsilon_b = 200\gamma_{a_i}$.

dissertation I will consider the following inequality developed by *Olsen*, *Bradley* and *Reid* [17]:

$$\mathrm{OBR}_{ijk} + \mathrm{OBR}_{jki} + \mathrm{OBR}_{kij} \geq 1, \tag{4.4}$$

where

$$\mathrm{OBR}_{ijk} \equiv V_{\mathrm{inf}}^{(t)}[\hat{X}_i] V_{\mathrm{inf}}^{(t)}[\hat{Y}_i], \tag{4.5}$$

and the tripartite inferred variances are defined as [18]

$$\mathrm{V}_{\mathrm{inf}}^{(t)}[\hat{X}_i] = \mathrm{V}[\hat{X}_i] - \frac{\left(\mathrm{C}[\hat{X}_i, \hat{X}_j + \hat{X}_k]\right)^2}{\mathrm{V}[\hat{X}_j + \hat{X}_k]}, \qquad \mathrm{V}_{\mathrm{inf}}^{(t)}[\hat{Y}_i] = \mathrm{V}[\hat{Y}_i] - \frac{\left(\mathrm{C}[\hat{Y}_i, \hat{Y}_j + \hat{Y}_k]\right)^2}{\mathrm{V}[\hat{Y}_j + \hat{Y}_k]}. \tag{4.6}$$

When (4.4) is violated, steering is demonstrated between the i, j and k modes. Steerable states are a strict subset of entangled states. The results for the three down converted modes are presented in Figure 4.4, where we see that they are entangled at low frequencies. The violation is slightly reduced in the pumped case. No violation of the inequality was found for any other combination of three modes, shown in Figure 4.5 for completeness. It is possible that they are still entangled, but steering is not exhibited.

4.3 Summary

We investigated the process of non-degenerate triplet down conversion by considering the spectrum of quadrature variances in the steady state for a single set of parameters. We found that all four modes are squeezed, and tripartite entanglement is exhibited between the three down converted modes. The squeezing of the b mode appears to be strongly dependent on the steady state of the a mode, as the inclusion of a small coherent signal to the a mode (via ϵ_a resulted in loss of b mode squeezing at zero frequency.

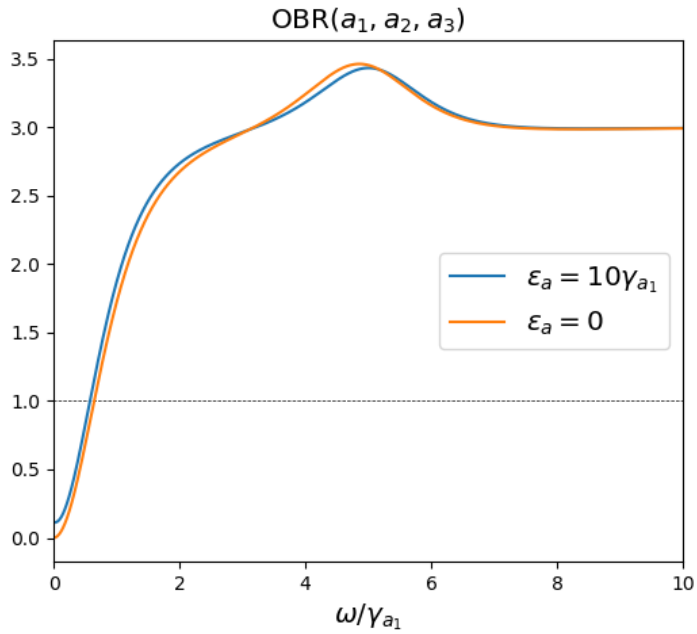

Figure 4.4: The spectrum of OBR_{123} in the cases when the a_1 and a_2 modes are pumped and not pumped in the steady state ($\epsilon_{a_1}, \epsilon_{a_2} = 10\gamma_{a_i}$ and 0 respectively). The dip below one around zero frequency indicates entanglement between the three down converted modes. The other parameters used are $\kappa = 0.001, \gamma_b = 2\gamma_{a_i}$, and $\epsilon_b = 200\gamma_{a_i}$.

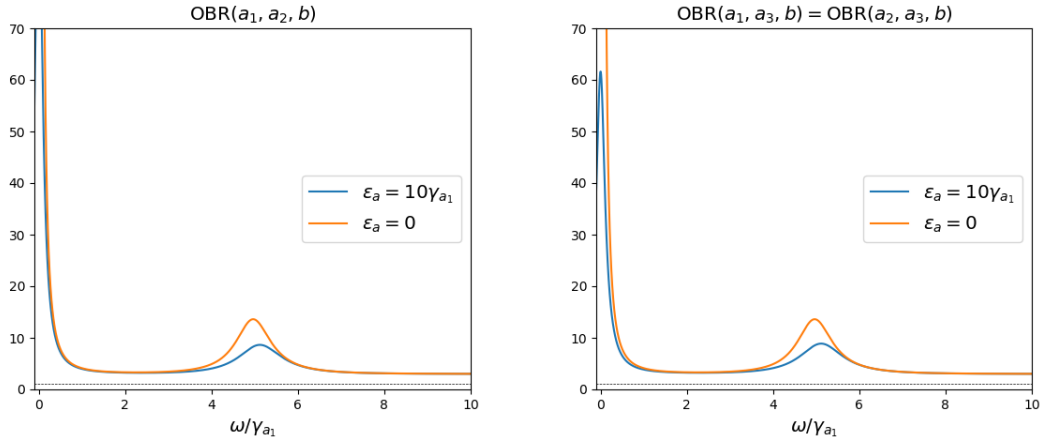

Figure 4.5: The spectra of OBR_{12b} and $\text{OBR}_{13b} = \text{OBR}_{23b}$ in the cases when the a_1 and a_2 modes are pumped and not pumped in the steady state ($\epsilon_{a_1}, \epsilon_{a_2} = 10\gamma_{a_i}$ and 0 respectively). The other parameters used are $\kappa = 0.001, \gamma_b = 2\gamma_{a_i}$, and $\epsilon_b = 200\gamma_{a_i}$.

Chapter 5

Monte Carlo Wave Function Simulation

The focus of this dissertation has been the application of optical phase space methods to investigate the process of triplet down conversion. Phase space has been used because the field produced by a highly stable laser operating well above its lasing threshold is exactly a coherent state, so they provide a convenient representation for quantum optical systems compared to, say, a number state basis. However, the positive-P SDEs that I have simulated throughout this dissertation are not exact, and the results I have obtained could differ from the physical process of triplet down conversion due to some key points at which errors may have been introduced. The first is that I am describing a physical process using a mathematical model which includes some approximations. Ultimately only comparison to experiments can determine the accuracy of the model, although it should be noted that master equations in Linblad form successfully describe many quantum optical systems under the correct approximations. Secondly, when mapping the master equation (1.56) into phase space we truncate the third order derivatives of the resulting PDE in order to make the mapping to an SDE. One way this has manifested itself is that down conversion would not proceed from the vacuum in my simulations without the addition of pumping to the a modes. This is not a physical result, but it is currently unclear how much of an effect the truncation actually has on the time evolution, and resulting steady states. The discrepancies associated with this procedure have not been examined in the literature, and are the topic of this chapter. Finally, the errors associated with numerically simulating the coupled SDEs (1.59) are dealt with in Appendix B.

In this section I compare truncated positive-P simulations to simulations of the master equation (1.56) for the same system in a number state basis. This is a desirable comparison because direct simulations of (1.56) will provide us with insight into the effect of the truncation on the accuracy of the truncated positive-P simulations. However, it is first beneficial to note why we could justify truncating the third order therm in the first place. This comes down to a simple scaling argument as follows. First of all, we note that the phase space variables scale with the square root of the number of photons, as can be seen in (1.26). We then define the scaled phase space variable $\tilde{\alpha}$ such that

$$\alpha = \tilde{\alpha}\sqrt{n}, \tag{5.1}$$

and the same for the other three phase space variables. Substituting these into the Fokker-Planck

equation for triplet down conversion, (1.57), we obtain

$$\begin{aligned}\frac{\partial \tilde{P}}{\partial t} = -\Bigg[&\frac{1}{\sqrt{n}}\frac{\partial}{\partial\tilde{\alpha}}(n^{3/2}\kappa\tilde{\alpha}^{+2}\tilde{\beta}) + \frac{1}{\sqrt{n}}\frac{\partial}{\partial\tilde{\alpha}^{+}}(n^{3/2}\kappa\tilde{\alpha}^{2}\tilde{\beta}^{+}) + \frac{1}{\sqrt{n}}\frac{\partial}{\partial\tilde{\beta}}\left(-\frac{n^{3/2}\kappa}{3}\tilde{\alpha}^{3}\right)\\ &+\frac{1}{\sqrt{n}}\frac{\partial}{\partial\tilde{\beta}^{+}}\left(-\frac{n^{3/2}\kappa}{3}\tilde{\alpha}^{+3}\right) - \frac{1}{\sqrt{n}}\frac{\partial}{\partial\tilde{\alpha}}(\sqrt{n}\gamma_a\tilde{\alpha}) - \frac{1}{\sqrt{n}}\frac{\partial}{\partial\tilde{\alpha}^{+}}(\sqrt{n}\gamma_a\tilde{\alpha}^{+})\\ &+\frac{1}{\sqrt{n}}\frac{\partial}{\partial\tilde{\beta}}(\epsilon_b) + \frac{1}{\sqrt{n}}\frac{\partial}{\partial\tilde{\beta}^{+}}(\epsilon_b^{*})\Bigg]\tilde{P}(\tilde{\alpha},\tilde{\alpha}^{+},\tilde{\beta},\tilde{\beta}^{+}).\\ &+\frac{1}{2}\left[\frac{1}{n}\frac{\partial^2}{\partial\tilde{\alpha}^{2}}(2n\kappa\tilde{\alpha}^{+}\tilde{\beta}) + \frac{1}{n}\frac{\partial^2}{\partial\tilde{\alpha}^{+2}}(2n\kappa\tilde{\alpha}\tilde{\beta}^{+})\right]\tilde{P}(\tilde{\alpha},\tilde{\alpha}^{+},\tilde{\beta},\tilde{\beta}^{+}).\\ &-\frac{1}{3}\left[\frac{1}{n^{3/2}}\frac{\partial^3}{\partial\tilde{\alpha}^{3}}(\sqrt{n}\kappa\tilde{\beta}^{+}) + \frac{1}{n^{3/2}}\frac{\partial^3}{\partial\tilde{\alpha}^{+3}}(\sqrt{n}\kappa\tilde{\beta})\right]\tilde{P}(\tilde{\alpha},\tilde{\alpha}^{+},\tilde{\beta},\tilde{\beta}^{+}).\end{aligned} \tag{5.2}$$

where we could take $P(\boldsymbol{\alpha}) \to \tilde{P}(\tilde{\boldsymbol{\alpha}})$ due to its linear nature. The important point to note is the overall powers of n in each term. Those corresponding to first order derivatives scale with between $n^{-1/2}$ and n; the second order terms are constant with respect to n; and the third order terms both scale with $n^{-1/2}$. Obviously for small numbers of photons the third order term will be important, but it will become decreasingly important as the size of the systems increases. This indicates that truncation is plausible in the classical limit of many photons that is used throughout this dissertation. This claim is examined below via comparison to a Monte Carlo wave function technique.

5.1 Monte Carlo Wave Function Techniques

It would be possible to directly simulate the time evolution of the density matrix subject to the master equation (1.56), but this is not the approach taken here. Instead we use the Monte Carlo wave function (MCWF) technique implemented in `QuantumOptics.jl`[1]. For an N-dimensional Hilbert space, the MCWF approach simulates the time evolution of an N-dimensional state rather than of an N^2-dimensional density matrix. The technique was developed in the 1990s for numerically simulating dissipative systems, and can be applied to any system with a master equation in Linblad form, such as (1.56). The theory behind the technique is discussed in [7], but the key point is that it simulates individual trajectories, and in the stochastic average their time evolution can be used to recover the density matrix consistent with the master equation. A brief outline of the simulation of an individual trajectory is given below:

1. Given an initial state, time evolution is simulated according to the Schrödinger equation using the non-Hermitian Hamiltonian

$$\hat{H} - \frac{i\hbar}{2}\sum_i \hat{J}_i^{\dagger}\hat{J}_i, \tag{5.3}$$

[1] See https://qojulia.org/documentation/timeevolution/mcwf.html.

where the $\hat{J}_i$ are the jump operators that represent dissipative behaviour in the Linblad form of the master equation - in the context of triplet down conversion they are the annihilation operator for each mode.

2. At random times[2] there is a "quantum jump" to a different state given by

$$|\psi(t)\rangle \longrightarrow \frac{\hat{J}_i |\psi(t)\rangle}{\langle\psi(t)| \hat{J}_i^\dagger \hat{J}_i |\psi(t)\rangle}, \tag{5.4}$$

then time evolution proceeds as above. When the jump operator is an annihilation operator, this is equivalent to removing a photon from the system - it is modelling the damping of each mode.

The trade off with this technique is that we require a stochastic average over many trajectories, but this is usually still faster than simulating the full density matrix [7]. That being said, MCWF simulations using the parameters that have been used throughout this dissertation would require a Hilbert space that was prohibitively large for numeric simulations, because the expected number of photons in my simulations has been on the order of 10,000. Instead, we have limited ourselves to systems which have expected mode populations on the order of 100 photons. Note that the Hilbert space required to model this needs to be larger than the maximum expected number of photons because the actual state will be close to a coherent state, which has a Poissonian distribution in terms of the number states. We also focus on degenerate triplet down conversion.

In practice, because it requires a large Hilbert space, the MCWF method is still significantly slower than the truncated positive-P method. However, its lack of truncation provides a valuable check for the truncated positive-P results which has not been done before.

5.2 Results

For the purposes of comparison, I ran simulations of three sets of parameters, aiming to cover i) a system that reaches a steady state, ii) a system with interesting dynamics, and iii) a system that is located within the "transition region" (the noise terms - the second order derivatives in the Fokker-Planck equation - are dominant around the critical pumping, so it is to be expected that the same is true for the third order terms). The results are presented in Figures 5.1 - 5.3 respectively for phase space simulations averaged over 20,000 trajectories, and MCWF simulations averaged over 1,000 simulations. It should be noted that the phase space simulations took on the order of one minute to run, while the number state simulations were on the order of one to two days. A more detailed comparison in this respect is beyond the scope of this chapter.

We can see that on a whole the truncated positive-P technique matches the behaviour of the MCWF simulations fairly well, but there are some small systematic discrepancies. In Figures 5.1 and 5.3 the solutions appear to gain a constant offset, while in Figure 5.2 the frequency of the oscillations appears to be slightly altered. However, these results confirm that in general the truncation has a minimal effect. In Figure 5.3 in particular some of the discrepancy can be explained by noting that 1,000 trajectories is probably not enough for the simulations to converge for the given parameters.

[2]There is physics behind the probability of a quantum jump at any given time, but it is not relevant here.

There are a couple of additional points to make about the agreement between the simulations. Firstly, as noted above, the truncated positive-P simulations will be least accurate for low mode populations. It would be expected that the discrepancies are smaller for the parameters used throughout this dissertation. Secondly, due to the time involved with the simulations, an examination of the convergence of the number state simulations analogous to that in Appendix B for the phase space simulations has not been possible, but it is unlikely that they have converged after only 1,000 trajectories. Number state simulations averaged over more trajectories would likely, but not definitely, lead to stronger agreement with the phase space simulations.

Finally, it is worth noting that the key factor that affects the accuracy of the number state simulations, apart from the number of trajectories averaged over, are the sizes of the Hilbert spaces used for each mode. In order to confirm that the Hilbert spaces used in my simulations were large enough, I ran the same simulations for larger Hilbert spaces, and confirmed that the results did not change. For example, the Hilbert spaces used for the simulations presented in Figure 5.2 had dimensions of $N_a = 270$ and $N_b = 60$ for the a and b modes respectively. When increased significantly to $N_a = 310$ and $N_b = 100$ the results were unchanged. For the MCWF implementation in `QuantumOptics.jl`, all randomness is generated from a seed, so the comparison was made for individual trajectories.

5.3 Summary

A comparison between truncated positive-P phase space simulations and MCWF simulations in a number state basis was made for three systems with low photon populations. This is the first time such a comparison has been made. The results are largely consistent, supporting the use of the truncated positive-P method for investigating triplet down conversion.

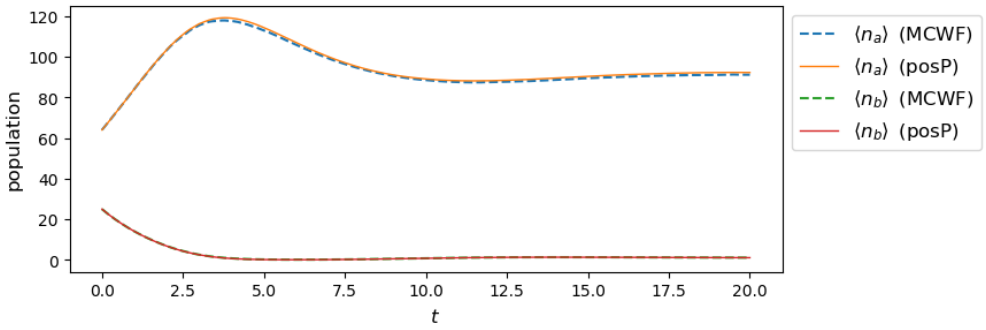

Figure 5.1: A comparison between the time evolution as given by the truncated positive-P SDE (1.59) and by the Monte Carlo wave function technique. The parameters used are $\kappa = 0.005, \gamma_a = 0.05, \gamma_b = 0.5, \epsilon_b = 2$, and $\epsilon_a = 0$. The SDE was averaged over 20,000 trajectories, while the MCWF was averaged over 1000 trajectories. The Hilbert spaces had dimensions of $N_a = 160$ and $N_b = 60$ for the a and b modes respectively.

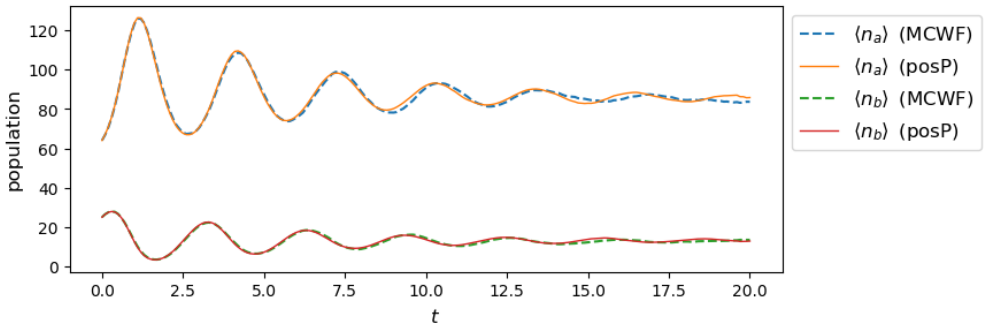

Figure 5.2: A comparison between the time evolution as given by the truncated positive-P SDE (1.59) and by the Monte Carlo wave function technique. The parameters used are $\kappa = 0.025, \gamma_a = 0.8, \gamma_b = 1, \epsilon_b = 11$, and $\epsilon_a = 0$. The SDE was averaged over 5000 trajectories, while the MCWF was averaged over 1000 trajectories. The Hilbert spaces had dimensions of $N_a = 270$ and $N_b = 90$ for the a and b modes respectively.

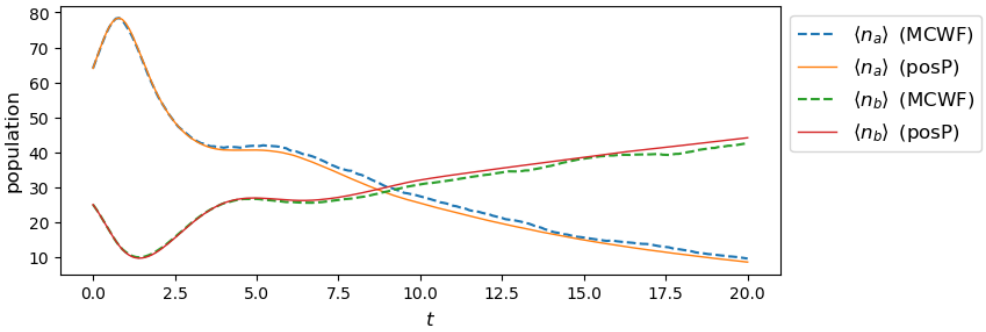

Figure 5.3: A comparison between the time evolution as given by the truncated positive-P SDE (1.59) and by the Monte Carlo wave function technique. The parameters used are $\kappa = 0.025, \gamma_a = 0.8, \gamma_b = 1, \epsilon_b = 8$, and $\epsilon_a = 0$. The SDE was averaged over 20,000 trajectories, while the MCWF was averaged over 1000 trajectories. The Hilbert spaces had dimensions of $N_a = 270$ and $N_b = 90$ for the a and b modes respectively.

Chapter 6

Conclusion

In this thesis we have performed a systematic numerical investigation of intra-cavity triplet down conversion using optical phase space methods. We have identified regimes of squeezing and entanglement in the accessible output fields for a pumped steady state. To do this we first obtained a clear understanding of the stable steady states of the mode populations. These were used to generate fluctuation spectra for the output fields, and to calculate a number of other measures related to experimentally accessible quantum information.

We began by mapping a master equation for degenerate triplet down conversion into optical phase space using a truncated positive-P method. The time evolution and steady states of the resulting stochastic differential equation were thoroughly analysed, including comparison to a semi-classical approximation. This comparison identified two critical regimes in which quantum fluctuations play a particularly important role. The first was a critical point in the time evolution at which rapid growth in the population of the low energy mode was observed. The quantum treatment indicated a reduced magnitude of this behaviour. The second was a critical pumping, defined as that at which the semi-classical approximation obtained steady states corresponding to a non-vacuum low energy mode. Far above, and below the critical pumping, the semi-classical approximation was consistent with the quantum treatment, but it was found that quantum noise effects can lead to shifted steady state populations about the critical pumping.

From these steady states we then systematically investigated the squeezing and entanglement of the output fields as a function of the high energy pumping that drove the interaction. It was found that the steady output fields were squeezed and entangled at all pump intensities above the critical pumping. Once again, the region around the critical pumping required a quantum treatment, which showed that squeezing of the low energy was most extreme around the critical pumping. Below critical pumping all modes are in a minimum uncertainty state.

As a generalisation of the degenerate results presented, we briefly considered the process of non-degenerate triplet down conversion. All four modes were found to be squeezed, and the three down converted modes were found to be tripartite-entangled and steerable. A strong dependence of the squeezing of the high energy mode on the steady state of the low energy mode was identified, but deeper conclusion require a more in-depth analysis.

A comparison of the truncated positive-P method to a Monte Carlo wave function method was made for the case of degenerate triplet down conversion. This was the first time such a comparison has been made, and it provided valuable insight into the effect of truncation on the results presented throughout this dissertation. Some small systematic discrepancies between the

methods were identified, but the overall results were in strong agreement, validating the use of a positive-P approach to triplet down conversion.

In summary, an in-depth analysis of the process of triplet down conversion has been performed in optical phase space. Physically important quantities and regimes have been identified and investigated, and the results validated via comparison with simulations in a number state basis. As the positive-P model is generally a reliable description of damped quantum optical systems, our results should offer a guide for experimental efforts to utilise triplet down conversion as a resource for quantum information applications.

References

[1] M. Olsen. Private communication, 2017.

[2] Jiri Bajer. Photon statistics of the Nth subharmonics. *Journal of Modern Optics*, 38(6):1085–1091, 1991.

[3] Hannes Hbel, Deny Hamel, Alessandro Fedrizzi, Sven Ramelow, Kevin J Resch, and Thomas Jennewein. Direct generation of photon triplets using cascaded photon-pair sources. 466:601–3, 07 2010.

[4] Mercedes Gimeno-Segovia, Pete Shadbolt, Dan E Browne, and Terry Rudolph. From three-photon Greenberger-Horne-Zeilinger states to ballistic universal quantum computation. 115:020502, 07 2015.

[5] Andrew M. Lance, Thomas Symul, Warwick P. Bowen, Barry C. Sanders, and Ping Koy Lam. Tripartite quantum state sharing. *Phys. Rev. Lett.*, 92:177903, Apr 2004.

[6] M Olsen, L Plimak, and Michael Fleischhauer. Quantum-theoretical treatments of three-photon processes. 65, 04 2002.

[7] Andrew J. Daley. Quantum trajectories and open many-body quantum systems. *Advances in Physics*, 63(2):77–149, 2014.

[8] V. Bužek. Reconstruction of Liouvillian superoperators. *ArXiv e-prints*, 58:1723–1727, September 1998.

[9] Crispin Gardiner and Peter Zoller. *Foundations of Quantum Optics*. Imperial College Press, 2nd edition, 2014.

[10] D.F. Walls and G.J. Milburn. *Quantum Optics*. Springer, 1994.

[11] Crispin Gardiner. *Stochasitc Methods*. Springer, 4th edition, 2009.

[12] C. W. Gardiner and P. D. Drummond. *Ten Years of the Positive P-Representation*, pages 77–86. Springer US, Boston, MA, 1993.

[13] David J. Griffiths. *Introduction to Electrodynamics*. Pearson, 4th, new international edition, 2014.

[14] C.W. Gardiner and M.J. Collett. Input and output in damped quantum systems: Quantum stochastic differential equations and the master equation. *Physical Review A*, 31(6), 1985.

[15] Lu-Ming Duan, G. Giedke, J. I. Cirac, and P. Zoller. Inseparability criterion for continuous variable systems. *Phys. Rev. Lett.*, 84:2722–2725, Mar 2000.

[16] R. Simon. Peres-Horodecki separability criterion for continuous variable systems. *Phys. Rev. Lett.*, 84:2726–2729, Mar 2000.

[17] M. K. Olsen, A. S. Bradley, and M. D. Reid. Continuous variable tripartite entanglement and EinsteinPodolskyRosen correlations from triple nonlinearities. *Journal of Physics B: Atomic, Molecular and Optical Physics*, 39(11):2515, 2006.

[18] A. S. Bradley, M. K. Olsen, O. Pfister, and R. C. Pooser. Bright tripartite entanglement in triply concurrent parametric oscillation. *Phys. Rev. A*, 72:053805, Nov 2005.

Appendix A

Notation

$\alpha, \beta, \alpha^+, \beta^+$	phase space variables; eigenvalues of coherent states
$\xi, \xi_i, \xi(t)$	a random variable, subject to the properties outlined in §1.4.2
$\|\psi\rangle, \langle\psi\|$	a ket and a bra representing a quantum mechanical state and its Dual vector respectively
$\mathbf{a}, \boldsymbol{\alpha}$	boldface indicates a vector quantity
$\hat{A}, \hat{a}$	an over-hat indicates an operator
$\dot{\alpha}$	the time derivative of α, equivalent to $\frac{d\alpha}{dt}$
α^*	the complex conjugate of α
$\|\alpha\|$	the absolute value of the complex number α
α_s	the steady state value of the variable α
$\hat{a}^\dagger$	the conjugate transpose (adjoint) of the operator $\hat{a}$, discussed in §1.1
$\hat{a}^T, A^T$	the transpose of the operator $\hat{a}$ or the matrix A
$\langle\hat{x}\rangle, \langle\hat{x}\rangle_\psi$	the expectation value of the operator $\hat{x}$, discussed in §1.1
$\overline{x}$	the expectation value of the stochastic variable x, discussed in §1.4.1
Δx	the standard deviation of the operator $\hat{x}$
$\mathrm{V}[x]$	the variance of x, defined in §1.4.1
$\mathrm{C}[x, y]$	the covariance between x and y, defined in §1.4.1

Appendix B

Numerics

Even if the SDEs (1.59) (and (4.2)) modelled the process of triplet down conversion exactly, there will still be errors associated with the results obtained from numerical simulations. Firstly, simulating (1.59) only recovers the result of its corresponding FPE exactly in the limit that we average over infinite trajectories. We need to ensure that enough trajectories have been averaged over in order for the simulations to have converged. Secondly, there are the usual numerical issues relating to discretisation - primarily the time step used in the simulations.

B.1 Averaging over Trajectories

I begin by considering the effect that the number of trajectories averaged over has on the simulations. To begin, Figure B.1 shows the steady state value given by the average of between 1 and 30,000 trajectories for an ensemble of ten different simulations, and the variance of these values. We see that after approximately 5,000 trajectories agreement between simulations barely improves, which is to say that the simulations have converged. At this point the simulations differ from each other by less than 0.05%, which is extremely good agreement. However, this does not necessarily imply that the simulations have converged on a whole, nor is it surprising that the steady states are in such agreement - in Section 2.1 we showed that the semi-classical ODE had steady states fairly consistent with individual stochastic trajectories. The only source of error in the steady states is the relatively small stochastic terms, so not many trajectories are required to average them away.

In order to quantify the convergence of the overall simulation, Figure B.2 shows the the largest range of values at any time across the ten simulations for each "number of trajectories averaged over". Unsurprisingly, this does not converge as fast or as well as the steady states, but importantly it does appear to level off around 15,000 trajectories - and in fact most of the variation is gone by 5,000 trajectories. Most importantly, there is no obvious improvement after 20,000 trajectories.

B.2 Tolerances

I will now consider the effect of the step size on the simulations. Throughout my work I used the `LambaEulerHeun` algorithm[1], which uses an adaptive step size, so rather than being set directly, the step size is determined at each time step by a relative and absolute error tolerance passed to

[1] See http://docs.juliadiffeq.org/latest/solvers/sde_solve.html#Full-List-of-Methods-1.

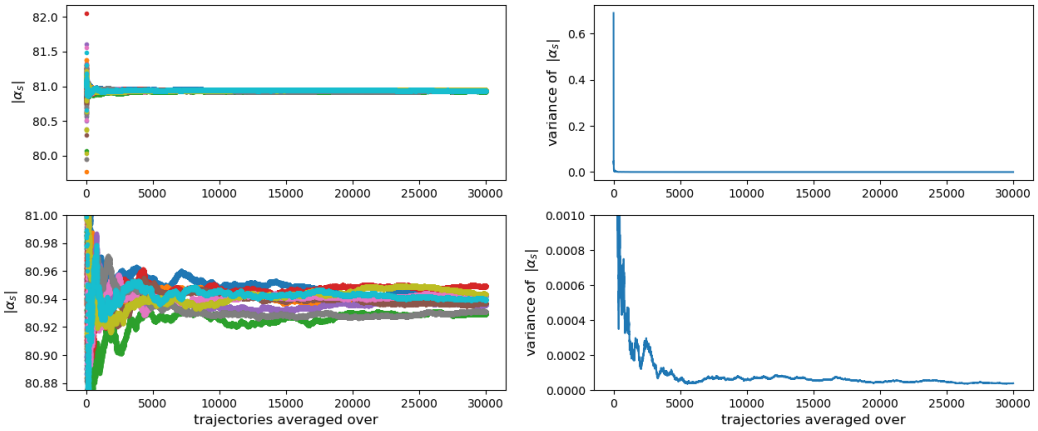

Figure B.1: The convergence of the steady state values as more trajectories are averaged over. LEFT: The value of $|\alpha_s|$ obtained from ten different simulations. RIGHT: The variance of the values of $|\alpha_s|$ given by the ten simulations. The parameters used are $\kappa = 0.001, \gamma_b = 2\gamma_a, \epsilon_a = 5\gamma_a$, and $\epsilon_b = 200\gamma_a$.

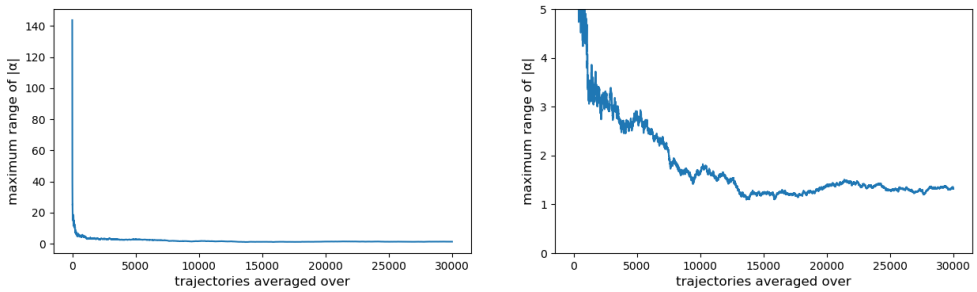

Figure B.2: The largest range of values of $|\alpha|$ at any time across ten simulations as a function of the number of trajectories averaged over. The parameters used are $\kappa = 0.001, \gamma_b = 2\gamma_a, \epsilon_a = 5\gamma_a$, and $\epsilon_b = 200\gamma_a$.

the solver[2]. A smaller tolerance will result in an overall smaller step size. In my simulations I used the default absolute and relative tolerances of 10^{-2}.

In order to investigate the role of the tolerances, ten simulations were run for tolerances ranging from $10^{-0.5}$ to 10^{-4}. For each simulation the absolute and relative tolerances were set to the same value, and averaged over 20,000 trajectories. Figure B.3 shows the effect this had on the steady states. We see that by around $10^{-1.5}$ the solution has converged. It is interesting to note that for the larger tolerances the steady states are predicted to be smaller than the converged value. By $10^{-1.5}$ the variance of $|\alpha_s|$ has also levelled off, indicating that decreasing the tolerance further does not improve the solution. In terms of the overall time evolution, the tolerances were found to have no effect, at least when averaging over 20,000 trajectories. Ultimately the steady states are the most important however, as they are the quantity that was used to determine the key results presented in Chapters 2 and 3.

[2]See http://docs.juliadiffeq.org/latest/basics/common_solver_opts.html#Stepsize-Control-1.

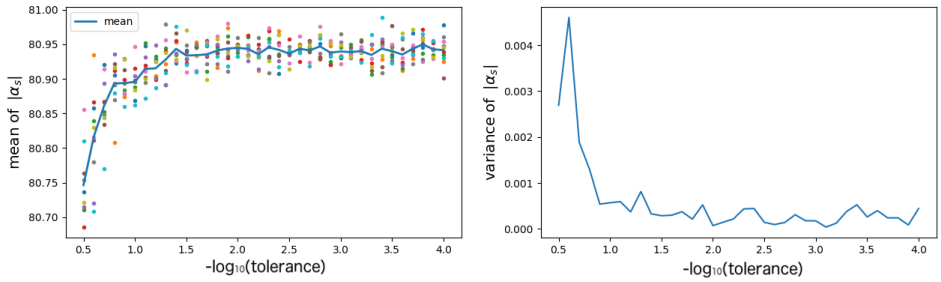

Figure B.3: The convergence of the steady state values as a function of the tolerances passed to the SDE solver LEFT: The steady state values of $|\alpha_s|$ predicted by ten simulations. RIGHT: The variance of steady state values of $|\alpha_s|$ given by the ten simulations. The parameters used are $\kappa = 0.001, \gamma_b = 2\gamma_a, \epsilon_a = 5\gamma_a$, and $\epsilon_b = 200\gamma_a$, and 20,000 trajectories were averaged over.

B.3 Batching Trajectories

As a final note, we briefly discuss the details of the simulations. In the simulations presented throughout this dissertation, phase space variables were averaged over 20,000 trajectories. This has been shown to be enough to converge, but has the unfortunate downside of being too many to be held in RAM at once on the computer running the simulations, which slows down the computation significantly. In order to speed up calculations, we batched trajectories, which is to say we ran multiple Monte Carlo simulations of a relatively small number of trajectories, then averaged over these in order to obtain my final values. We tended to run 40 batches of 500 trajectories, which was a sufficiently small number of trajectories to remain in RAM.

Appendix C

Key Derivations

C.1 The von Neumann Master Equation

The von Neumann equation, introduced in Section 1.2.2, describes the time evolution of the density matrix for a closed system. It appears to take the form of a Heisenberg equation of motion for an operator, but actually differs by a factor of -1. The similarity is deceptive because the density matrix is defined explicitly in terms of state kets and bras, which undergo Schrödinger time evolution. From the definition of the density matrix, $\rho = \sum_n P_n |\psi_n\rangle \langle\psi_n|$, we see that its derivation requires the time evolution kets and bra. State kets undergo time evolution dictated by the Schrödinger equation. Rearranging (1.8) and taking its conjugate transpose yields the time evolution of a ket and a bra respectively as

$$\frac{\partial |\psi\rangle}{\partial t} = -\frac{i}{\hbar}\hat{H}|\psi\rangle\,, \qquad \text{and} \qquad \frac{\partial \langle\psi|}{\partial t} = \frac{i}{\hbar}\langle\psi|\hat{H},$$

where we used the fact that the Hamiltonian is Hermitian. The time evolution of the density matrix is then given by

$$\begin{aligned}
\frac{\partial}{\partial t}\sum_n P_n |\psi_n\rangle\langle\psi_n|\,, &= \sum_n P_n \left[\left(\frac{\partial |\psi_n\rangle}{\partial t}\langle\psi_n|\right) + \left(|\psi_n\rangle \frac{\partial \langle\psi_n|}{\partial t}\right)\right], \\
&= \sum_n P_n \left[-\frac{i}{\hbar}\hat{H}|\psi_n\rangle\langle\psi_n| + \frac{i}{\hbar}|\psi_n\rangle\langle\psi_n|\hat{H}\right], \\
&= -\frac{i}{\hbar}\sum_n P_n \left[\hat{H}, |\psi_n\rangle\langle\psi_n|\right] = -\frac{i}{\hbar}[\hat{H},\rho].
\end{aligned}$$

C.2 Definition of the Coherent States in terms of Number States

Defining the coherent states is motivated by considering the eigenstates of the annihilation operator $\hat{a}$. To calculate these, it stands to reason to use a number state basis as we know the action of $\hat{a}$ on $|n\rangle$, and they form a complete orthonormal basis. Denoting a potential eigenstate of $\hat{a}$ as $|\alpha\rangle$, we have

$$|\alpha\rangle = \sum_n c_n |n\rangle\,,$$

where the c_n coefficients are determined by taking the inner product between $\hat{a}\,|\alpha\rangle$ and the number state $|m\rangle$:

$$\begin{aligned}
\langle m|\,\hat{a}\sum_n c_n\,|n\rangle &= \langle m|\,\alpha\sum_{n'} c_{n'}\,\big|n'\big\rangle\,,\\
\sum_n \sqrt{n}\,c_n\,\langle m|n-1\rangle &= \sum_{n'}\alpha c_{n'}\,\big\langle m\big|n'\big\rangle\,,\\
\sum_n \sqrt{n}\,\delta_{m,n-1} &= \sum_{n'}\alpha c_{n'}\delta_{m,n'},\\
c_{m+1}\sqrt{m+1} &= \alpha\,c_m.
\end{aligned}$$

This defines the coefficients recursively, i.e.

$$c_n = \frac{\alpha}{\sqrt{n}}c_{n-1} = \frac{\alpha^2}{\sqrt{n(n-1)}}c_{n-2} = \ldots = \frac{\alpha^n}{\sqrt{n!}}c_0 \qquad \Longrightarrow \qquad |\alpha\rangle = \sum_n \frac{\alpha^n}{\sqrt{n!}}c_0.$$

In order to determine c_0 we normalise $|\alpha\rangle$ to obtain

$$\langle\alpha|\alpha\rangle = \sum_m\sum_n \frac{\alpha^{*n}}{\sqrt{n!}}\frac{\alpha^m}{\sqrt{m!}}\,\langle n|m\rangle\,|c_0|^2 = \sum_n \frac{|\alpha|^{2n}}{n!}|c_0|^2 = 1,$$

where $\sum_n \frac{x^n}{n!} = e^x$, so we have $|c_0| = e^{-|\alpha|^2/2}$. The overall phase is unimportant, so we can take $c_0 = |c_0|$, which gives us

$$|\alpha\rangle = e^{-|\alpha|^2/2}\sum_n \frac{\alpha^n}{\sqrt{n!}}\,|n\rangle\,.$$

C.3 Action of Creation Operator on a Coherent State

The actions of the creation and annihilation operators on coherent kets and bras are presented in 1.3.4. As an example, I derive $\hat{a}^\dagger\,|\alpha\rangle$ - as given by (1.28). Substituting in $|\alpha\rangle$ of the form (1.21), we obtain

$$\begin{aligned}
\hat{a}^\dagger\left(e^{-|\alpha|^2/2}\sum_n \frac{\alpha^n}{\sqrt{n!}}\,|n\rangle\right) &= e^{-|\alpha|^2/2}\sum_{n=0}^{\infty}\frac{\alpha^n}{\sqrt{n!}}\sqrt{n+1}\,|n+1\rangle\,, \qquad \text{let } m = n+1,\\
&= e^{-|\alpha|^2/2}\sum_{m=1}^{\infty}\frac{\alpha^{m-1}}{\sqrt{(m-1)!}}\sqrt{m}\,|m\rangle\,,
\end{aligned}$$

where $\sqrt{m}/\sqrt{(m-1)!} = m/\sqrt{m!}$, and the summation over m can begin from 0 since this term will not contribute to the sum

$$= e^{-|\alpha|^2/2}\sum_{m=0}^{\infty}\frac{m\alpha^{m-1}}{\sqrt{m!}}\,|m\rangle\,.$$

Notice that $m\alpha^{m-1}$ looks like a derivative with respect to α. We can calculate $\frac{\partial}{\partial\alpha}|\alpha\rangle$ via the product rule as

$$\frac{\partial}{\partial\alpha}\left(e^{-\alpha\alpha^*/2}\sum_n\frac{\alpha^n}{\sqrt{n!}}|n\rangle\right)=-\frac{\alpha^*}{2}\left(e^{-\alpha\alpha^*/2}\sum_n\frac{\alpha^n}{\sqrt{n!}}|n\rangle\right)+\left(e^{-\alpha\alpha^*/2}\sum_n\frac{n\alpha^{n-1}}{\sqrt{n!}}|n\rangle\right),$$

which is to say

$$\frac{\partial}{\partial\alpha}|\alpha\rangle=-\frac{\alpha^*}{2}|\alpha\rangle+\hat{a}^\dagger|\alpha\rangle\implies\hat{a}^\dagger|\alpha\rangle=\left(\frac{\alpha^*}{2}+\frac{\partial}{\partial\alpha}\right)|\alpha\rangle.$$

C.4 P Function Correspondences

The operator correspondences for the positive-P function are given in Section 1.3.7. In this appendix I derive the correspondence equivalent to (1.41) for the *P function*, which take on the same form, but with $\alpha^*\to\alpha^+$. Although it may not appear obvious, it can be formally shown that the same results are obtained for the positive-P function. We begin by applying the creation operator to the density matrix in the form (1.34). We use (1.28) to obtain

$$\begin{aligned}\hat{a}^\dagger\rho&=\int d^2\alpha\,P(\alpha,\alpha^*)\,\hat{a}^\dagger|\alpha\rangle\langle\alpha|,\\&=\int d^2\alpha\,P(\alpha,\alpha^*)\left(\frac{\alpha^*}{2}|\alpha\rangle+\frac{\partial}{\partial\alpha}|\alpha\rangle\right)\langle\alpha|,\\&=\int d^2\alpha\,P(\alpha,\alpha^*)\left(\frac{\alpha^*}{2}|\alpha\rangle\langle\alpha|+\frac{\partial|\alpha\rangle}{\partial\alpha}\langle\alpha|\right).\end{aligned}$$

We can replace the last term by considering the derivative of $|\alpha\rangle\langle\alpha|$ with respect to α

$$\frac{\partial}{\partial\alpha}[|\alpha\rangle\langle\alpha|]=\frac{\partial|\alpha\rangle}{\partial\alpha}\langle\alpha|+|\alpha\rangle\frac{\partial\langle\alpha|}{\partial\alpha}=\frac{\partial|\alpha\rangle}{\partial\alpha}\langle\alpha|-|\alpha\rangle\frac{\alpha^*}{2}\langle\alpha|.$$

Rearranging, and substituting back into the integral, we obtain

$$\begin{aligned}\hat{a}^\dagger\rho&=\int d^2\alpha\,P(\alpha,\alpha^*)\left(\alpha^*|\alpha\rangle\langle\alpha|+\frac{\partial}{\partial\alpha}[|\alpha\rangle\langle\alpha|]\right),\\&=\int d^2\alpha\,P(\alpha,\alpha^*)\,\alpha^*|\alpha\rangle\langle\alpha|+\int d^2\alpha\,P(\alpha,\alpha^*)\frac{\partial}{\partial\alpha}[|\alpha\rangle\langle\alpha|],\end{aligned}$$

where the derivative of $\langle\alpha|$ was calculated from the definition of $|\alpha\rangle$ in terms of number states. Applying integration by parts to the second term, and dropping the resulting boundary terms[1], we obtain

$$\begin{aligned}\hat{a}^\dagger\rho&=\int d^2\alpha\,P(\alpha,\alpha^*)\,\alpha^*|\alpha\rangle\langle\alpha|-\int d^2\alpha\,\frac{\partial P(\alpha,\alpha^*)}{\partial\alpha}|\alpha\rangle\langle\alpha|,\\&=\int d^2\alpha\left(\alpha^*-\frac{\partial}{\partial\alpha}\right)P(\alpha,\alpha^*)|\alpha\rangle\langle\alpha|.\end{aligned}$$

From this we observe the operator correspondence

$$\hat{a}^\dagger\rho\longleftrightarrow\left(\alpha^*-\frac{\partial}{\partial\alpha}\right)P(\alpha,\alpha^*).$$

[1]This is not possible in every case, which does limit the situations in which the P representation is useful, although in practice the boundary terms almost always vanish.

Appendix D

Additional Results

D.1 Effect of the Initial State on the Steady States

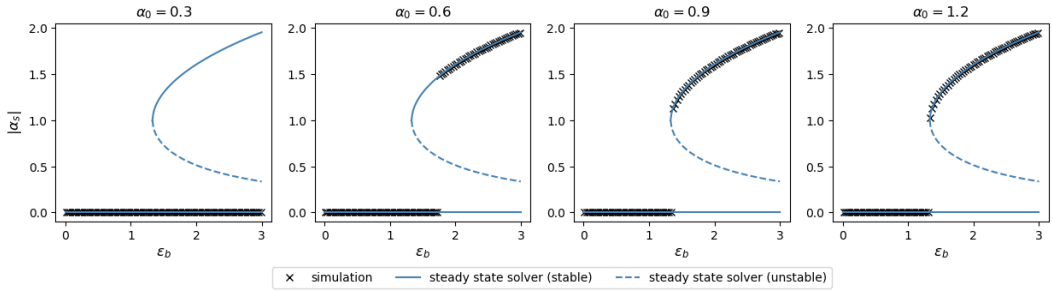

Figure D.1: The steady state values of $|\alpha|$ as a function of ϵ_b for four different initial states, as given by integration of (2.2). The parameters used are $\kappa = 0.001, \gamma_a = 1$, and $\gamma_b = 2$, and the $\alpha_0 = 1.2$ plot is a replication of Figure 2.4(b).

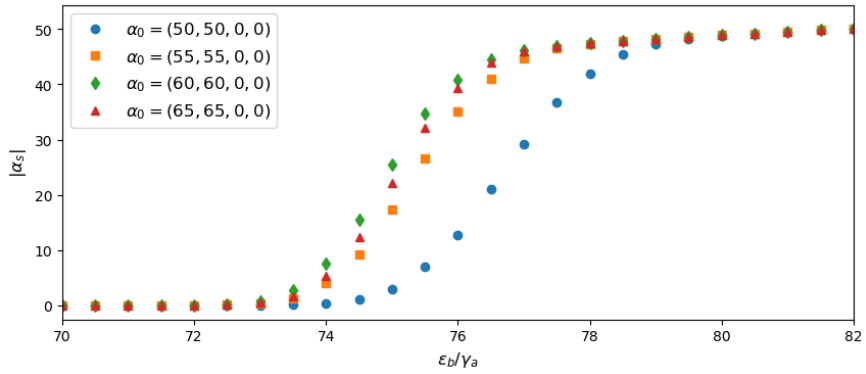

Figure D.2: The steady state values of $|\alpha|$ as a function of ϵ_b for four different initial states, as given by stochastic integration of (1.59) until $\gamma_a t = 150$. The parameters used are $\kappa = 0.001, \gamma_a = 1$, and $\gamma_b = 2$, 20,000 trajectories are averaged over, and the $\alpha_0 = 60$ solutions are a replication of those in Figure 2.6.

D.2 Steady States of $|\beta|$ as a Function of ϵ_b

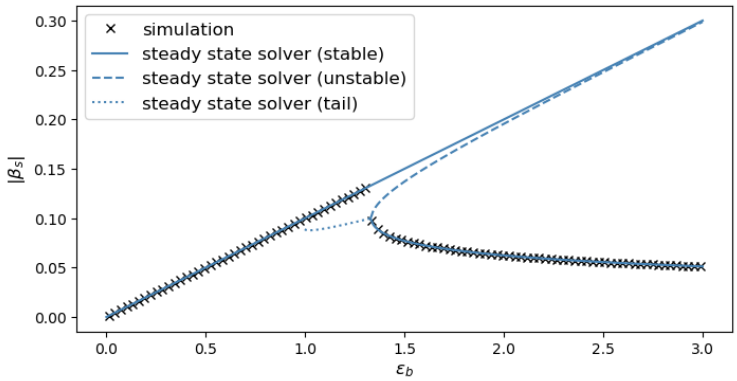

Figure D.3: The steady states of $|\beta|$ corresponding to the numerical results presented in Figure 2.4(b)

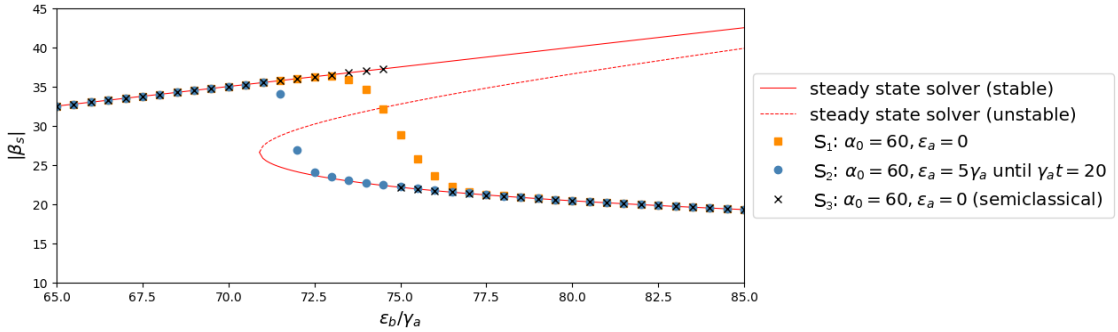

Figure D.4: The steady states of $|\beta|$ corresponding to the numerical results presented in Figure 2.6

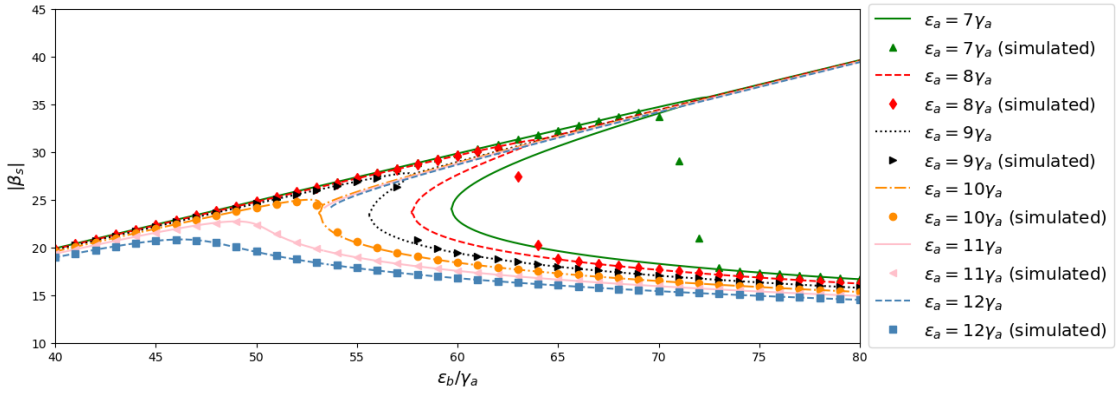

Figure D.5: The steady states of $|\beta|$ corresponding to the numerical results presented in Figure 2.9.

D.3 Time Evolution of $|\beta|$ as a Function of ϵ_b

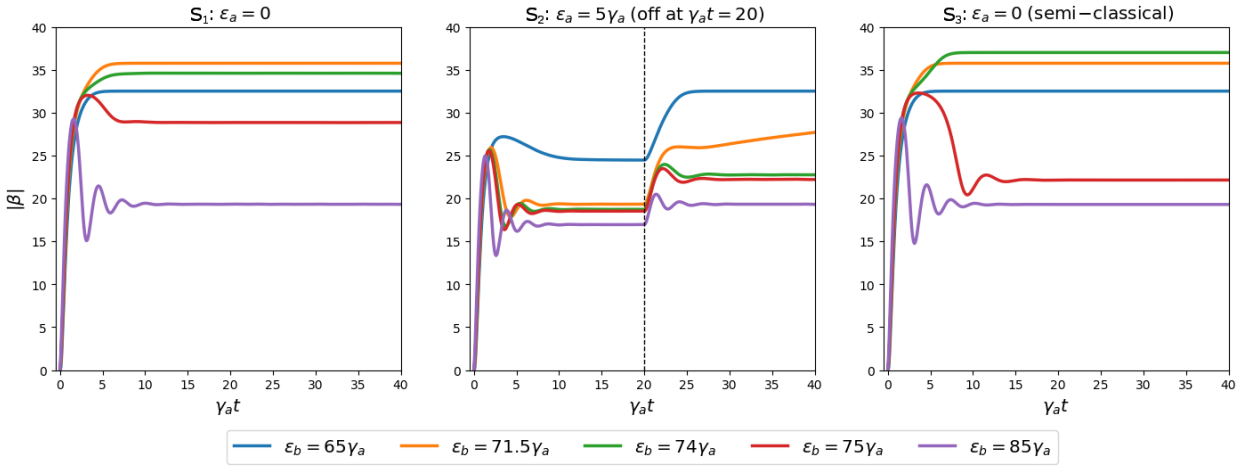

Figure D.6: The time evolution of $|\beta|$ corresponding to the numerical results presented in Figure 2.8.